J. Fluid Mech. (2010), *vol.* 643, *pp.* 1–31.
doi:10.1017/S0022112009991881

Drag and lift forces on particles in a rotating flow

J. J. BLUEMINK[1], D. LOHSE[1]†, A. PROSPERETTI[1,2] AND L. VAN WIJNGAARDEN[1]

[1]Faculty of Science and Technology and J. M. Burgers Centre for Fluid Dynamics, University of Twente, PO Box 217, 7500 AE Enschede, The Netherlands

[2]Department of Mechanical Engineering, The John Hopkins University, Baltimore, MD 21218, USA

(Received 23 December 2008; revised 29 August 2009; accepted 31 August 2009; first published online 17 December 2009)

A freely rotating sphere in a solid-body rotating flow is experimentally investigated. When the sphere is buoyant, it reaches an equilibrium position from which drag and lift coefficients are determined over a wide range of particle Reynolds numbers ($2 \leqslant Re \leqslant 1060$). The wake behind the sphere is visualized and appears to deflect strongly when the sphere is close to the cylinder axis. The spin rate of the sphere is recorded. In fluids with low viscosity, spin rates more than twice as large as the angular velocity of the cylinder can be observed. By comparing numerical results for a fixed but freely spinning sphere with a fixed non-spinning sphere for $Re \leqslant 200$, the effect of the sphere spin on the lift coefficient is determined. The experimentally and numerically determined lift and drag coefficients and particle spin rates all show excellent agreement for $Re \leqslant 200$. The combination of the experimental and numerical results allows for a parameterization of the lift and drag coefficients of a freely rotating sphere as function of the Reynolds number, the particle spin and the location of the particle with respect to the cylinder axis. Although the effect of the flow rotation on the particle spin is different in shear flow and solid-body rotating flow, the effect of spin on lift is found to be comparable for both types of flow.

Key words: particle/fluid flows

1. Introduction

The parameterization of lift and drag forces in non-uniform flows is a long-standing problem in fluid dynamics. A complex flow can be broken up into typical flows such as a uniform flow, a strain flow and a (solid-body) rotating flow. In this paper we consider a sphere in the last type of flow, and we experimentally measure the lift and drag forces on the sphere.

The flow is obtained by rotating a horizontal liquid-filled cylinder around its axis with constant angular velocity ω. Gravity is perpendicular to the rotation axis (figure 1*a*). The sphere is buoyant and reaches a stable equilibrium position at which all forces balance (see figure 1*b*). The total force on the sphere consists of a part that is due to buoyancy and gravity, drag, lift, inertia (or pressure gradient) and added mass. The last two forces are relevant even in this steady situation of a particle in its equilibrium position, as a result of the spatial acceleration of the undisturbed ambient flow. We obtain the steady-state drag and lift by measuring the equilibrium position. Furthermore we measure the particle spin rate. The same arrangement was used for

† Email address for correspondence: lohse.jfm@tnw.utwente.nl

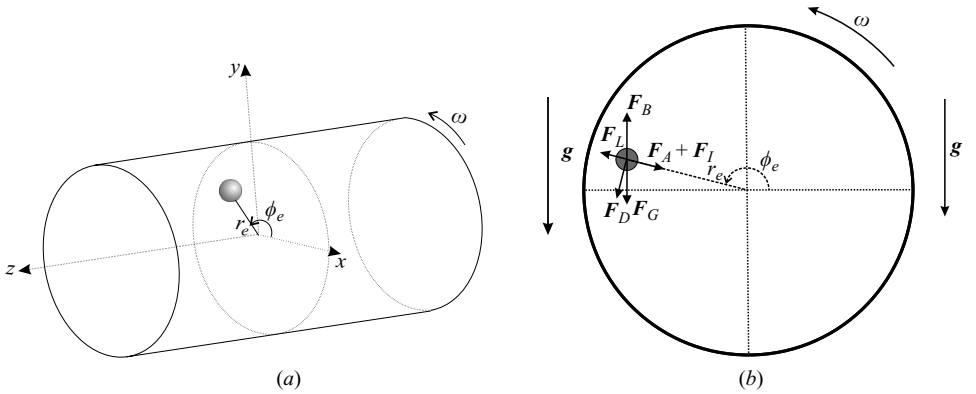

FIGURE 1. (*a*) Geometry of a sphere in a rotating cylinder. Here the cylinder rotates counterclockwise with constant angular velocity ω. (*b*) Force balance; $\boldsymbol{F}_G$ represents the gravitational force and $\boldsymbol{F}_B$ the buoyancy force; $\boldsymbol{F}_D$ is the drag force, $\boldsymbol{F}_L$ the lift force, $\boldsymbol{F}_A$ the added mass force and $\boldsymbol{F}_I$ the inertial or pressure gradient force.

studying an air bubble in Naciri (1992), Bluemink *et al.* (2005) and Van Nierop *et al.* (2007) and recently in Rastello *et al.* (2009). The set-up presently considered has a larger diameter (by a factor of 5) compared with that in Van Nierop *et al.* (2007) so that wall effects are far less likely to influence the results and relative errors can be reduced by considering equilibrium positions farther away from the cylinder axis.

This paper builds on the work of Bluemink *et al.* (2008) in which we discussed the spin rate of a sphere in several flow types and numerically determined lift and drag coefficients for a fluid in solid-body rotation. We observed an increase in the lift force due to the particle spin, further discussed in § 2.3. We use the results of Bluemink *et al.* (2008) and extend the analysis. From the numerical results, we show here the possibility to split the lift force in a part that is due to the flow and a part that is due to the particle spin, and we apply this to the experimental results.

In the experimental system we study a free sphere kept into place mainly by a balance between buoyancy and drag. Therefore the present situation has some resemblance to that of a light particle rising at constant velocity in a stationary fluid, described by Jenny, Bouchet & Dušek (2003) and Jenny, Dušek & Bouchet (2004), among others. From these results we know that a sphere displays path instability and will not follow a rectilinear path for a sufficiently high Reynolds number (Karamanev, Chavarie & Mayer 1996; Jenny *et al.* 2003, 2004; Veldhuis *et al.* 2005). This may affect the observations in our experiment. Path instability is coupled with wake instability (Mougin & Magnaudet 2002). In a uniform flow the wake behind a particle is steady and axisymmetric up to $Re \approx 212$. From $212 < Re < 274$ the wake is still steady but non-axisymmetric, though there is planar symmetry.

Several authors have studied the trajectory of particles in fluids in solid-body rotation. A full survey is given in Bluemink *et al.* (2008); here we mention in particular the experimental results of Candelier, Angilella & Souhar (2004, 2005, Shaw *et al.* 2006), where the behaviour of particles and bubbles falling and rising in a system with a vertical rotation axis was studied and the lift force was determined.

Bagchi & Balachandar (2002*b*) simulated a sphere spinning freely in a solid-body rotating fluid. However, as shown in Bluemink *et al.* (2008), their results for particle spin and lift are different from our experimental and numerical results for the same flow type.

The remainder of this paper is structured as follows. In § 2 we address the forces and revisit the numerical results for a solid-body rotating flow of Bluemink *et al.* (2008). We parameterize the lift for a spinning and a non-spinning sphere and analyze the influence of the spin on the lift force. Section 3 addresses the experiments in detail and compares the experimental results with the previously obtained numerical results. In § 4 we state the main conclusions of this paper.

2. Modelling of the forces on the sphere

In this section we consider the forces on the sphere and revisit the numerical results for a freely spinning sphere with a fixed centre reported in Bluemink *et al.* (2008). In that paper the spin rate of a sphere under torque-free conditions in several types of flow was considered. The reader is referred to that work for numerical details. In this section we will address the solid-body rotating flow, and in particular we will study the difference in lift coefficient for a non-spinning sphere and a freely spinning sphere and extend the analysis of these results. To render this paper self-contained some definitions and results of Bluemink *et al.* (2008) are repeated.

The situation is different from the experiment, since the particle centre is pinned in the numerical simulations. However, we expect no difference in behaviour for free and fixed spheres, since the numerical simulations are in the regime $Re \leqslant 200$ and thus below the critical Reynolds number at which the particle trajectory of a freely rising sphere deviates from a straight vertical line. When reaching Reynolds numbers above 200 we may expect the dynamics of the particle to change drastically as a result of path instability.

2.1. *Effective forces*

For a sphere at moderate-to-large Reynolds number subject to a gravitational field, a widely used equation of motion is (Magnaudet & Eames 2000; Mazzitelli, Lohse & Toschi 2003)

$$(\rho C_A + \rho_p) V \frac{\mathrm{d}\boldsymbol{v}}{\mathrm{d}t} = \rho V (C_A + 1) \frac{\mathrm{D}\boldsymbol{U}}{\mathrm{D}t} + \rho V C_L (\boldsymbol{U} - \boldsymbol{v}) \times (\boldsymbol{\nabla} \times \boldsymbol{U}) + \frac{1}{2} \rho C_D A |\boldsymbol{U} - \boldsymbol{v}| (\boldsymbol{U} - \boldsymbol{v}) + (\rho_p - \rho) V \boldsymbol{g}, \quad (2.1)$$

where $\boldsymbol{v}$ is the sphere velocity, $\boldsymbol{g}$ the gravitational acceleration, ρ the liquid density (greater than ρ_p the density of the sphere), V the sphere volume and A the cross-sectional area of the sphere; $\boldsymbol{U}$ is the velocity of the undisturbed ambient flow taken at the centre of the sphere; C_A is the added mass coefficient and has the value $1/2$ for a sphere; C_D and C_L are the drag and the lift coefficient. The lift force as included in (2.1) assumes that lift is only due to vorticity. It is well known (see e.g. Jenny *et al.* 2003, 2004) that wake instability also generates lift in the absence of flow vorticity. The results to be described below imply that this is a minor effect over most of our parameter range, which is further diminished by the averaging procedure that we follow in determining the equilibrium position of the sphere.

2.2. *Direct numerical simulation results revisited and governing simulation parameters*

To describe the numerical simulations of the flow past a sphere of radius R immersed in a solid-body rotational flow it is convenient to adopt a slightly different coordinate system from the one depicted in figure 1(*b*). Since, experimentally, the angle ϕ is found to be very close to π in the parameter range covered by the simulations, we

place the sphere on the y-axis and shift the origin to its centre. In this new coordinate system the undisturbed flow at the centre of the sphere is given by

$$\boldsymbol{U}(x, y) = -\omega y \hat{\boldsymbol{e}}_x + (\omega x - U_0)\hat{\boldsymbol{e}}_y, \tag{2.2}$$

in which $-U_0$ is the undisturbed velocity at the centre of the sphere, corresponding to ωr_e in the polar coordinates of figure 1(b).

The relevant dimensionless numbers which can be set in the numerical simulations are the particle Reynolds number

$$Re = \frac{2RU_0}{\nu}, \tag{2.3}$$

with ν the dynamic viscosity of the fluid, and the vorticity parameter

$$Sr_\omega = \frac{2\omega R}{U_0}, \tag{2.4}$$

which non-dimensionalizes the flow vorticity 2ω.

As response parameters we will consider the lift and drag coefficients and the particle spin rate. The drag coefficient C_D and the lift coefficient C_L, which are for the position of the sphere in the simulations in respectively the vertical and the horizontal direction, are obtained by balancing the forces in (2.1) in the x-direction and the y-direction defined by (2.2),

$$F_y = (\rho - \rho_p)Vg + \frac{1}{2}C_D\rho\pi R^2 U_0^2, \tag{2.5}$$

$$F_x = \rho V C_L[\boldsymbol{U} \times (\nabla \times \boldsymbol{U})] \cdot \hat{\boldsymbol{e}}_x + \rho V(C_A + 1)[\boldsymbol{U} \cdot \nabla \boldsymbol{U}] \cdot \hat{\boldsymbol{e}}_x. \tag{2.6}$$

2.3. *Decoupling the spin-induced lift from the flow-induced lift*

The numerical results in Bluemink *et al.* (2008) were obtained with the direct numerical simulation (DNS) method Physalis (Zhang & Prosperetti 2005), a combination of a finite-difference and a spectral method. Figure 2 shows the drag and lift coefficients for a sphere in a solid-body rotating flow as functions of the Reynolds number, with the vorticity parameter $Sr_\omega = 0.1$. The numerical results for the drag coefficient (figure 2a) show good agreement with a much-used standard drag curve (solid line) for uniform flow,

$$C_D = \frac{24}{Re}(1 + 0.15Re^{0.687}), \tag{2.7}$$

(Clift, Grace & Weber 1978), even though the flow is not uniform. The open symbols indicate non-rotating spheres and the closed symbols freely rotating ones. It is clear that the spin has only a tiny effect on the drag coefficient.

The computation of the lift coefficient is more delicate than that of the drag coefficient. Since there are not many data points with which we can compare our results for a sphere in a solid-body rotating flow, the finite-volume code Jadim (Magnaudet, Rivero & Fabre 1995; Legendre & Magnaudet 1998) was used to validate the Physalis results by simulating non-rotating spheres. For details on the method, see Magnaudet *et al.* (1995) and Legendre & Magnaudet (1998). We used $100 \times 56 \times 34$ nodes in the (ξ, η, ϕ) directions respectively. Both methods yield comparable results for the lift coefficient of a non-rotating sphere (open symbols in figure 2b), indicating that the Physalis results for non-rotating spheres are reliable. A fit through the Physalis data for a non-rotating sphere in the regime $20 \leqslant Re \leqslant 200$

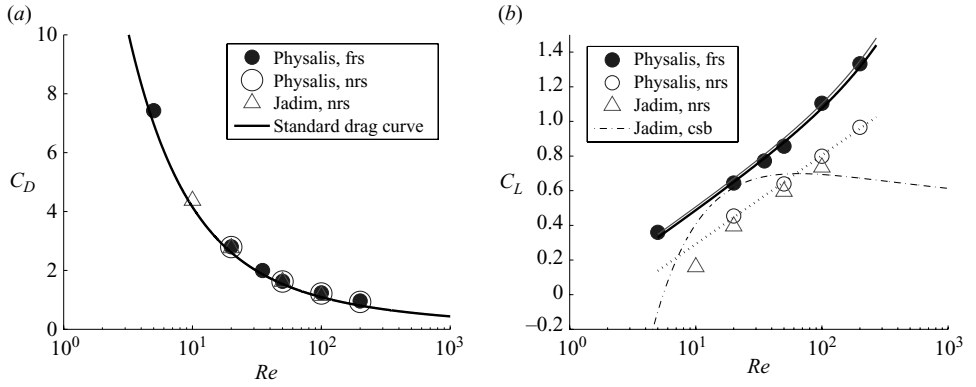

FIGURE 2. Numerical results for C_D and C_L for a sphere in a rotating flow obtained with two different numerical codes; $Sr_\omega = 0.1$ for all cases. Physalis data are from Bluemink *et al.* (2008). The abbreviations 'frs', 'nrs' and 'csb' stand for freely rotating sphere, non-rotating sphere and clean spherical bubble. (*a*) Drag coefficient versus Reynolds number. (*b*) Lift coefficient versus Reynolds number. The dotted line is the fit (2.8) through the Physalis data of a non-rotating sphere. The solid line is the combination (2.15) of (2.8) and the contribution that is due to the Magnus-like lift (2.14). The thinner line just above is a similar combination of the fits with (2.12) of Bagchi & Balachandar (2002*a*) instead of (2.14). The fit for a clean spherical bubble is taken from Magnaudet & Legendre (1998).

yields

$$C_{L,nrs} = 0.51 \log_{10} Re - 0.22, \tag{2.8}$$

with $C_{L,nrs}$ the lift coefficient for a non-rotating sphere.

For freely rotating spheres the lift coefficient is higher because a Magnus-like lift contribution is added owing to the sphere spin. The sphere spins freely and adopts the spin rate dictated by the condition of zero torque. It affects the lift force as indicated by the numerical work of e.g. Kurose & Komori (1999), Bagchi & Balachandar (2002*a*) and Bluemink *et al.* (2008). For a sphere spinning with an imposed angular velocity Ω in a uniform flow at small Reynolds number Rubinov & Keller (1961) calculated lift and drag forces, accurate to terms $O(Re)$. They found for the lift to this order

$$\boldsymbol{F}_L = \rho\pi R^3 \boldsymbol{\Omega} \times \boldsymbol{U}. \tag{2.9}$$

We cannot expect to be able to add a similar contribution to the lift force on our freely spinning sphere, since we are in a Reynolds number regime in which superposition is not allowed. However, we can expect the lift force to increase as the sphere spin increases. Lin, Peery & Schowalter (1970) calculated for a simple shear flow that the torque-free spin rate of a sphere decreases as the inertial effect increases. In contrast with that are the results of Bluemink *et al.* (2008), where a sphere in a solid-body rotating flow was found to spin faster as the inertial effect increased. Therefore the spin has a significant effect on the lift force at higher Reynolds number in a solid-body rotating flow.

Most DNS results for lift and drag have been obtained for particles in a linear shear flow, for example Dandy & Dwyer (1990), Kurose & Komori (1999) and Bagchi & Balachandar (2002*a*). All these results show that the lift coefficient decreases as the Reynolds number increases. Dandy & Dwyer (1990) simulated a fixed non-rotating sphere in a linear shear flow at different shear rates. Kurose & Komori (1999) simulated rotating and non-rotating spheres in a linear shear flow for $1 \leqslant Re \leqslant 500$.

They found a change in the sign of the lift coefficient for non-rotating spheres at $Re = 60$, with the lift force acting from the low-fluid-velocity side to the high-fluid-velocity side below $Re = 60$. At high Reynolds numbers they could not separate the lift force into a part owing to shear and a part owing to sphere spin, since in their view the flow separation is strongly affected by both shear and rotation. It should be noted that their sphere spin rate was imposed. Bagchi & Balachandar (2002*a*) allowed the sphere to rotate freely and in contrast found that they could decouple the Magnus-like lift (because of particle spin) and the shear-induced lift in the range $0.5 \leqslant Re \leqslant 200$, i.e.

$$\boldsymbol{F}_L(Re, Sr, \Omega_P) = \boldsymbol{F}_L(Re, Sr = 0, \Omega) + \boldsymbol{F}_L(Re, Sr, \Omega = 0). \tag{2.10}$$

Here $\boldsymbol{F}_L(Re, Sr, \Omega_P)$ is the lift on a freely spinning sphere in a shear flow with dimensionless shear rate Sr; $\boldsymbol{F}_L(Re, Sr = 0, \Omega)$ is the lift on a sphere in a uniform flow with imposed spin rate Ω (the torque-free spin rate that the sphere would attain in a shear flow with Sr); and $\boldsymbol{F}_L(Re, Sr, \Omega = 0)$ is the lift on a non-spinning sphere in a shear flow with Sr. They approximated the Magnus-like lift due to the shear-induced spin by

$$\boldsymbol{F}_L(Re, Sr = 0, \Omega_P) = \boldsymbol{F}_{L,Mg} \approx 0.55\rho\pi R^3 \Omega_P \times \boldsymbol{U}, \tag{2.11}$$

i.e. 55 % of the Rubinov & Keller (1961) result for a sphere with an imposed spin in a uniform flow. With (2.6) as the definition for C_L the contribution that is due to the sphere spin on the lift coefficient according to Bagchi & Balachandar (2002*a*) in (2.11) is

$$C_L(Re, Sr = 0, \Omega_P) = C_{L,Mg} \approx 0.55\frac{3}{8}\frac{\Omega_P}{\omega}. \tag{2.12}$$

As indicated by Bagchi & Balachandar (2002*a*) the decoupling is possible when the particle spins freely. The lift effects behave linearly in this case up to a much higher Reynolds number than observed by Kurose & Komori (1999). They expected the decoupling to be valid over a Reynolds range much wider than they considered. Rastello *et al.* (2009) used tracer particles and showed that a bubble surface spins in the solid-body rotating flow. They used their measured spin rates in combination with (2.11) to explain the increased lift they measured as a result of that spinning.

In our numerical results the normalized spin rate for a particle in rotating flow is fitted, as a function of Re, for $Re \leqslant 200$ as (see the results in Bluemink *et al.* 2008)

$$\frac{\Omega_P}{\omega} = 1 + 0.0045Re. \tag{2.13}$$

Adding the Magnus-like lift to the lift coefficient for non-rotating spheres should result in the lift coefficient for spinning spheres, if the effects behave linearly as indicated in (2.10). Similar to (2.12) the data in figure 2(*b*) show that a good fit (for $Re \leqslant 200$) for the spinning sphere is obtained if a contribution for the Magnus-like lift of

$$C_{L,Mg} \approx 0.5\frac{3}{8}\frac{\Omega_P}{\omega} \approx \frac{3}{16}\frac{\Omega_P}{\omega} \tag{2.14}$$

is added. The lift coefficient then depends on Re as

$$C_L = C_{L,nrs} + \frac{3}{16}\frac{\Omega_P}{\omega} = 0.51\log_{10} Re - 0.22 + \frac{3}{16}(1 + 0.0045Re). \tag{2.15}$$

The thick solid line in figure 2(*b*) represents (2.15). The thinner line above it is the same fit with (2.12) instead of (2.14) to model the contribution of the Magnus-like lift.

The numerical data for a freely rotating sphere in figure 2(*b*) show good agreement with (2.15). We can therefore conclude that in the range $5 \leqslant Re \leqslant 200$ the effects of the Magnus-like lift and the lift induced by the flow can be decoupled in the same fashion as (2.10) for this rotating flow. We also find that the factor by which the Magnus-like lift should be multiplied before it is added to the flow-induced lift is very close to that found by Bagchi & Balachandar (2002*a*) for linear shear flow. These findings are remarkable, since the behaviour of the sphere spin in a linear shear flow is totally different from that in a solid-body rotating flow. Yet the effect on the lift force is the same. The dash-dotted line in figure 2(*b*) represents a fit of the data of Magnaudet & Legendre (1998) for a clean spherical bubble in a liquid in solid-body rotation. It is clear that these curves show a completely different trend. Since the bubble is not allowed to deform in the simulation, this difference is solely due to different boundary conditions at the surface.

3. Experiments

3.1. *Governing parameters*

The governing parameters of the experimental system are the gravitational acceleration $\boldsymbol{g}$, the liquid viscosity ν, the liquid density ρ, the particle density ρ_p, the particle radius R and the cylinder angular velocity ω. Three independent dimensionless groups can be formed from these parameters, for example

$$Ta = \frac{2R^2\omega}{\nu}, \qquad Ga = \frac{2R\sqrt{2R(1-\rho_p/\rho)g}}{\nu}, \qquad \frac{\rho_p}{\rho}, \tag{3.1}$$

in which Ta is the Taylor number, Ga the Galilei number and ρ_p/ρ the density ratio. Note that the Galilei number and the density ratio are the dimensionless control parameters in the system of a freely falling and rising sphere studied by Jenny *et al.* (2003, 2004). Their observations may thus be relevant for our system.

The quantities measured in the experiments are the equilibrium position of the sphere (r_e, ϕ_e) and its spin rate Ω_P. The equilibrium position allows us to determine the lift and drag coefficients. The spin rate is measured because it has a significant influence on the lift coefficient.

The relationship between the equilibrium position of the sphere and the lift and drag coefficients is obtained by setting $\boldsymbol{v} = \mathrm{d}\boldsymbol{v}/\mathrm{d}t = 0$ and $\boldsymbol{U} = \omega r_e \hat{\boldsymbol{e}}_\phi$ with r_e as shown in figure 1(*b*). After decomposing the buoyancy force in the radial and angular directions, solving the equation of motion (2.1) gives

$$\tan\phi_e = \frac{8}{3}\frac{R}{C_D r_e}(2C_L - 1 - C_A), \tag{3.2}$$

$$r_e = -\frac{g(\rho-\rho_p)\sin\phi_e}{\rho\omega^2(2C_L - 1 - C_A)}. \tag{3.3}$$

Equations (3.2) and (3.3) can be solved to see the effect of the governing parameters on the equilibrium position r_e of the particle. If the drag coefficient is estimated by $C_D = 24/Re$, r_e can be expressed as

$$r_e = \frac{R^2(\rho-\rho_p)g}{\rho\omega\sqrt{(81/4)\nu^2 + R^4\omega^2(2C_L - 1 - C_A)^2}}. \tag{3.4}$$

For very viscous fluids, $\nu \gg R^2\omega$, we find that the distance of the particle from the cylinder axis depends on the cylinder rotation rate as

$$\frac{r_e}{R} = 2\frac{(1-\rho_p/\rho)gR}{9\nu}\frac{1}{\omega} = \frac{1}{18}\frac{Ga^2}{Ta}, \tag{3.5}$$

whereas for fluids with a very low viscosity

$$\frac{r_e}{R} = \frac{(1-\rho_p/\rho)g}{R(2C_L-1-C_A)}\frac{1}{\omega^2} = \frac{1}{2}\frac{1}{(2C_L-1-C_A)}\frac{Ga^2}{Ta^2}. \tag{3.6}$$

The dependence of the drag coefficient C_D and the lift coefficient C_L on r_e and ϕ_e is (rewriting (3.2) and (3.3))

$$C_L = \frac{1}{2}\left[1 + C_A - \frac{\rho-\rho_p}{\rho}\frac{g\sin\phi_e}{r_e\omega^2}\right], \tag{3.7}$$

$$C_D = -\frac{8}{3}\frac{\rho-\rho_p}{\rho}\frac{R}{r_e^2 w^2}g\cos\phi_e. \tag{3.8}$$

Since the undisturbed velocity at the particle centre is $U_0 = \omega r_e$, r_e enters the Reynolds number (2.3) and the Froude number,

$$Re = \frac{2RU_0}{\nu} = \frac{2Rr_e\omega}{\nu}, \qquad Fr = \frac{U_0^2}{2Rg} = \frac{r_e^2\omega^2}{2Rg}, \tag{3.9}$$

and the vorticity parameter (2.4),

$$Sr_\omega = \frac{2\omega R}{U_0} = \frac{2R}{r_e}. \tag{3.10}$$

3.2. *Experimental set-up*

In the experiment a sphere is inserted in a horizontal cylinder filled with a liquid. The cylinder has a radius of 250 mm and a length of 500 mm (outer dimensions). Its wall and end caps are made of Plexiglas that is 15 mm thick. Two steel rods, with a rubber coating to prevent slip, support the cylinder, and a third rod is mounted above it. One of the rods is connected to an AC servo motor by a belt and drives the rotation. The cylinder rotates with frequencies between 0 and 2 revolutions s^{-1} or Hz; the rotation rate can be set precisely. The cylinder can be pivoted to an almost upright position for filling purposes. For the definition of the coordinates, see also figure 1(*a*). After the cylinder is set into rotation some time is allowed to reach a steady state.

The sphere position is determined by projecting its shadow on a screen (an opal diffusing glass plate of 200×250 mm). For this purpose a narrow laser beam is broadened into a parallel beam with a diameter of about 8 cm. The beam passes through the cylinder, creating a bright spot on the screen located at the other side of the cylinder (figure 3). A grid with 1 cm spacing is attached to the screen. The shadow of the particle on the grid is recorded with a camera at 50 fps. The camera is connected to a computer, and the position of the particle shadow with respect to the grid is determined by image analysis. The cylinder axis is determined by recording marks on its end caps for a full rotation. These marks trace circles whose centres, determined by image analysis, give the position of the centres of the end caps with respect to the grid. Measuring the location of the sphere along the cylinder axis and linearly interpolating the centres of the end caps with respect to the grid provides the position of the cylinder axis at the axial plane of the sphere with respect to the grid,

Liquid number	Percentage of glycerine (by weight)	ν mm^2 s^{-1}	ρ_l g cm^{-3}	Re range	Symbol in figures	Uncertainty Re	Uncertainty Sr_ω	Uncertainty C_D	Uncertainty C_L
1	89	170.1	1.232	1.8–1.9	□	4 %	2 %	5 %	>100 %
2	85	91.1, 86.0	1.222	5.2–5.5	▲ and △	3 %	1 %	4 %	50 %
3	80	55.2	1.211	11.0–11.5	■	4 %	1 %	4 %	20 %
4	75	28.1	1.194	24.7–29.9	◇	4 %	2 %	5 %	10 %
5	68	15.4	1.174	59.9–68.0	►	4 %	1 %	3 %	10 %
6	60	9.3	1.154	107–127	◆	10 %	1 %	3 %	10 %
7	48	4.5, 4.8	1.121	234–297	▼ and ▽	4 %	1 %	4 %	10 %
8	30	2.3	1.071	450–574	★	4 %	2 %	4 %	10 %
9	0	0.98	0.997	687–1060	◄ and ◁	3 %	2 %	4 %	10 %

TABLE 1. Properties of the experimental liquids and order of magnitude of the uncertainties for the different liquids.

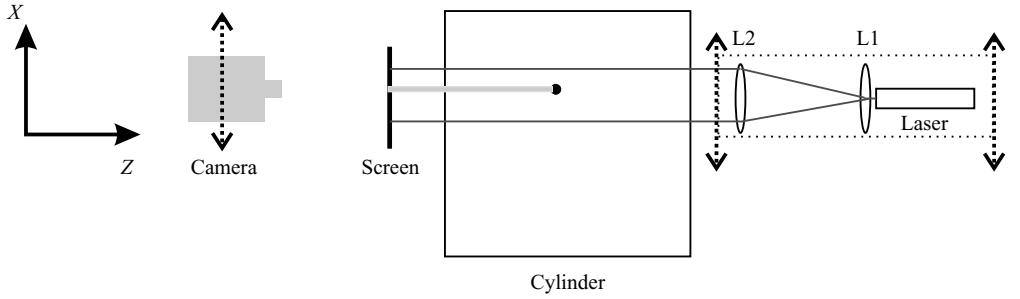

FIGURE 3. Top view of the optical parts of the experimental set-up; L1 is a lens with f = 10 mm, and L2 is a lens with f = 1000 mm.

thus correcting for misalignment between the laser and the cylinder axis. Since there is no constraint for motion in the direction of the cylinder axis, the sphere may also move in the (axial) z-direction. However, that motion is over a much longer time scale compared to that in the xy-plane; it usually takes several minutes for the particle to translate from one end cap of the cylinder to the other, whereas the frequency of the circling motion coincides with that of the cylinder.

To cover a wide range of Reynolds numbers, nine mixtures of glycerine and water with different viscosities were prepared. Table 1 shows the different liquids, together with the mass percentage of glycerine. It also shows the kinematic viscosity, the fluid density and the Reynolds range covered by each liquid. The viscosity was measured by means of several U-tube and Ubbelohde viscometers, and the density was measured with a pycnometer. For some liquids two different viscosities, corresponding to different temperatures, are indicated in table 1. The temperature was monitored and recorded during the experiment, and the viscosity was determined at the same temperature.

To obtain a minimum excursion around the equilibrium position, a sphere with a density much lower than that of water is the best choice. However, such spheres are generally hollow and have an inhomogeneous mass distribution, or they are manufactured in such a way that sphericity is not assured. To have good sphericity and mass distribution, low-density polyethylene (LDPE) spheres with a radius of 3.97 mm and a density ratio of $\rho_p/\rho_{water} \approx 0.93$ were used. For the viscous fluids ρ_p/ρ

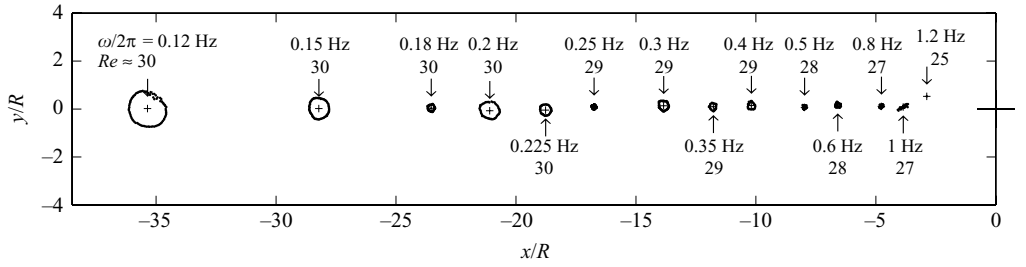

FIGURE 4. Particle trajectories for a sphere in liquid 4 (table 1) in the xy-plane. The cross at (0,0) is the cylinder axis. The position is normalized by the radius of the sphere. For each trajectory the cylinder rotation frequency $\omega/2\pi$ and the Reynolds number Re are indicated.

is smaller than for water (since these fluids have a higher density). As a result the equilibrium position is more stable for the lower-numbered liquids in table 1. To determine the spin rate, the sphere is marked and its spin is recorded by a video camera. In water (liquid 9 in table 1) the behaviour of a second sphere with a radius of 3.18 mm and a density ratio of $\rho_p/\rho_{water} \approx 0.94$ was also studied, although the spin rates were not measured. Measurements for this sphere are indicated by open triangles pointing to the left ($\triangleleft$).

The experimental procedure consists of filling the tank with one of the fluids and inserting the sphere. Bubbles initially remaining in the cylinder are removed by tilting the tank somewhat and rotating it slowly. The bubbles drift to a side of the cylinder, where they can be removed at an air inlet by adding fluid. When the tank is completely filled with fluid, the cylinder is tilted back to its horizontal position and set into rotation. Waiting times of 10 min up to 1 h may be needed for the spin-up of the fluid (for the estimate of spin-up times, see Bluemink *et al.* 2008) and to allow a particle to reach its equilibrium position and torque-free spin rate (which takes a long time especially in the case of highly viscous fluids).

An error analysis by propagating the errors in r_e, ϕ_e, ρ_b, R, ρ_l, ν and ω shows that for the liquids with high viscosity the measurement uncertainty of the lift coefficient is high. The error in the measurement of the position is estimated to be 1 mm in the x-direction and 0.5 mm in the y-direction for the experiments in which the particle displays only tiny excursions from its equilibrium position. For the measurements at which the sphere circles around its equilibrium position, the error in position was estimated to be a few millimetres in both directions. An error in the angle $\Delta\phi_e$ propagates strongly in the error of the lift coefficient. The error in the drag coefficient depends more strongly on the relative error in the radial distance from the cylinder axis $\Delta r_e/r_e$. In the last four columns of table 1 an indication of the measurement uncertainty for each liquid is shown. These values are a good representation for the measurement uncertainty of most data points.

3.3. *Results: particle trajectories*

Figures 4–7 show particle trajectories in liquids 4, 7, 8 and 9. For the definition of the xy-plane, see figure 1(a). In the figures the cylinder rotation frequency $\omega/2\pi$ and the Reynolds number Re are indicated for each trajectory. Figure 4 is a typical representation of the behaviour of the sphere in liquids 1–6. In these liquids the sphere remains more or less stationary at an equilibrium position. In some cases it makes a larger excursion around a fixed point. However, the trajectory it traces is

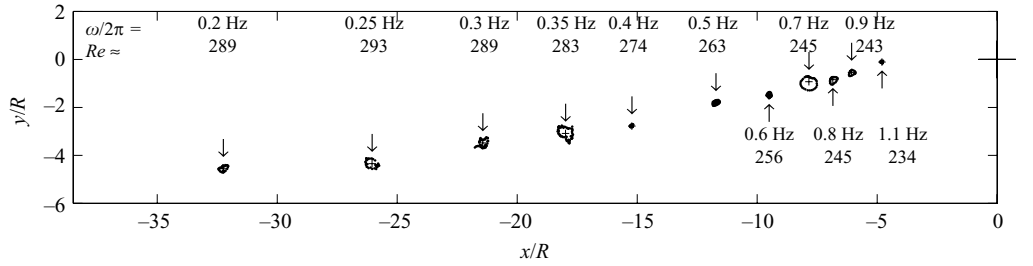

FIGURE 5. Particle trajectories for a sphere in liquid 7 (table 1) in the xy-plane. The cross at the very right at (0,0) is the cylinder axis; the direction of rotation is down in this region. The position is normalized by the radius of the sphere. For each trajectory the cylinder rotation frequency $\omega/2\pi$ and the Reynolds number Re are indicated.

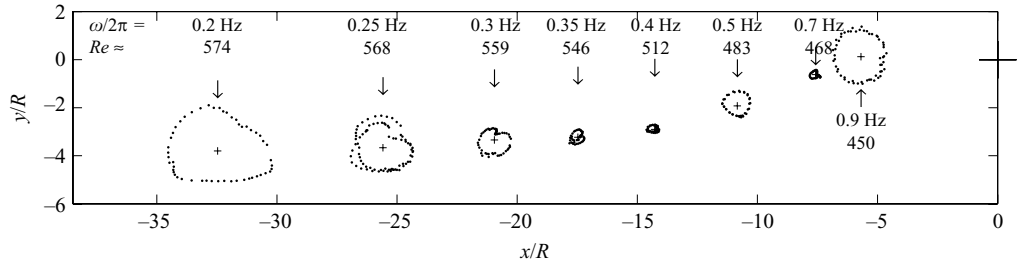

FIGURE 6. Particle trajectories for a sphere in liquid 8 (table 1) in the xy-plane. The cross at (0,0) is the cylinder axis. The position is normalized by the radius of the sphere. For each trajectory the cylinder rotation frequency $\omega/2\pi$ and the Reynolds number Re are indicated.

very regular and appears to be spiralling inward over several hours. We define the effective equilibrium position as the centre of the trajectory.

Figure 5 represents the trajectories in liquid 7 and shows the transition of the sphere resting in its equilibrium position (for the higher cylinder frequencies) to a somewhat erratic path around it (for the lower cylinder frequencies). For $Re \leqslant 274$ the trajectories are regular, and most of the time the radius of the trajectory is much smaller than the particle radius. For $Re \geqslant 283$ the trajectories become irregular and their radii are larger. Allowing a longer waiting time has no effect on the trajectory; the path remains erratic. The qualitative change in trajectories occurs between $Re = 274$ and $Re = 283$. Since this is close to the Reynolds number at which a particle in a quiescent fluid stops rising in a rectilinear motion and starts displaying spiralling or zigzag motion, this change in behaviour is probably connected to path instability (see § 1).

For liquids 8 and 9 ($Re \geqslant 450$; figures 6 and 7) Re is everywhere above this critical Reynolds number. Indeed, we observe that the particle trajectory has changed from small and nearly circular around the equilibrium position to a totally erratic path around a fixed point. In a quiescent fluid the deviation of a rising sphere from vertical motion is in any plane containing the gravitational acceleration. For the present rotating system, the sphere motion is principally in the xy-plane (the plane perpendicular to the background vorticity) shown in figures 6 and 7, i.e. the plane spanned by the gravitational and the centripetal acceleration.

When the sphere is close to the cylinder axis (i.e. the vorticity parameter Sr_ω is high) its trajectory is no longer erratic but a regular reproducible circle. When the

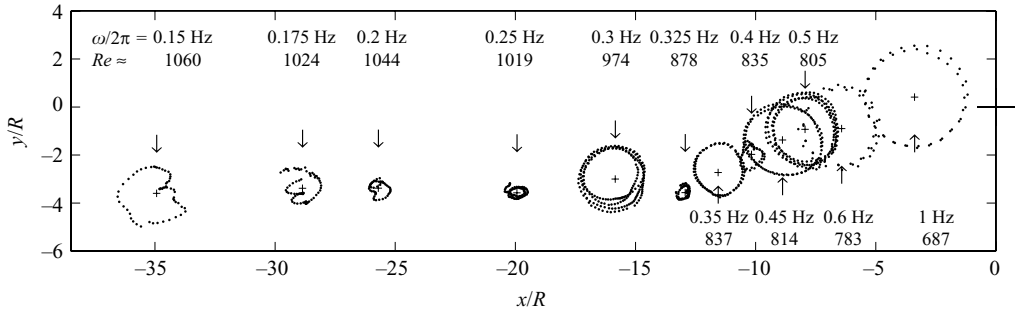

FIGURE 7. Particle trajectories for a sphere in liquid 9 (table 1) in the xy-plane. The cross at (0,0) is the cylinder axis. The position is normalized by the radius of the sphere. For each trajectory the cylinder rotation frequency $\omega/2\pi$ and the Reynolds number Re are indicated.

particle is followed for several periods, its path is observed to overlay itself. The circle travelled by the particle has a radius larger than twice the particle radius.

For Reynolds numbers larger than 274 wake dynamics causes fluctuating forces on the sphere, which have a nonlinear character and may result in limit cycles around a fixed point, instead of an equilibrium position. The effective equilibrium position is determined by taking the average over a complete cylinder rotation. The time needed for a full cylinder rotation equals the time needed for the sphere making a full circle around this effective equilibrium position; i.e. the cylinder rotation frequency and the sphere excursion frequency are the same for the regular trajectories. Averaging over the sphere trajectory is appropriate for the small trajectories or the trajectories that are located sufficiently far from the cylinder axis. However, for the large circular trajectories close to the cylinder axis it is unclear what flow field is seen by the particle. As a result the data with a high vorticity parameter are less reliable.

3.4. *Results: particle image velocimetry images of the sphere wake*

The phenomena discussed in § 3.3 are most probably a result of the wake structure behind the sphere. Since the sphere is held in its equilibrium position by a balance of forces, the situation is similar to a sphere rising freely at constant velocity. We expect to encounter the analogues of path and wake instability discussed in § 1. However, owing to rotation these instabilities may be different from those affecting a freely rising sphere at terminal velocity in a quiescent fluid. It is therefore of interest to study the wake behind the sphere in the solid-body rotating flow.

To visualize the flow around a particle, the fluid (water) was seeded with hollow glass spheres with a diameter of 15 μm. The wake in the xy-plane (figure 1a) was visualized by standard particle image velocimetry (PIV) measurements at cylinder rotation frequencies of 0.2, 0.5 and 1.0 Hz. The resulting flow fields (indicated by arrows) and vorticity fields (indicated by colour) can be seen in figures 8(a)–8(c). For each case we tried to determine the vortex shedding frequency. Vortices appear to be shed on both sides, but the shedding on the high-fluid-velocity side is more pronounced. This is in contrast with Sakamoto & Haniu (1995), who studied the wake of a fixed particle in a linear shear flow. They found that at the appearance of vortex shedding, vortex loops are detached always on the high-fluid-velocity side, in contrast to a uniform flow without shear, where the detachment point of the vortex loops alternates.

From the PIV results we cannot conclude with certainty that vortex shedding occurs solely in the xy-plane. However, since the circling motion in the xy-plane discussed

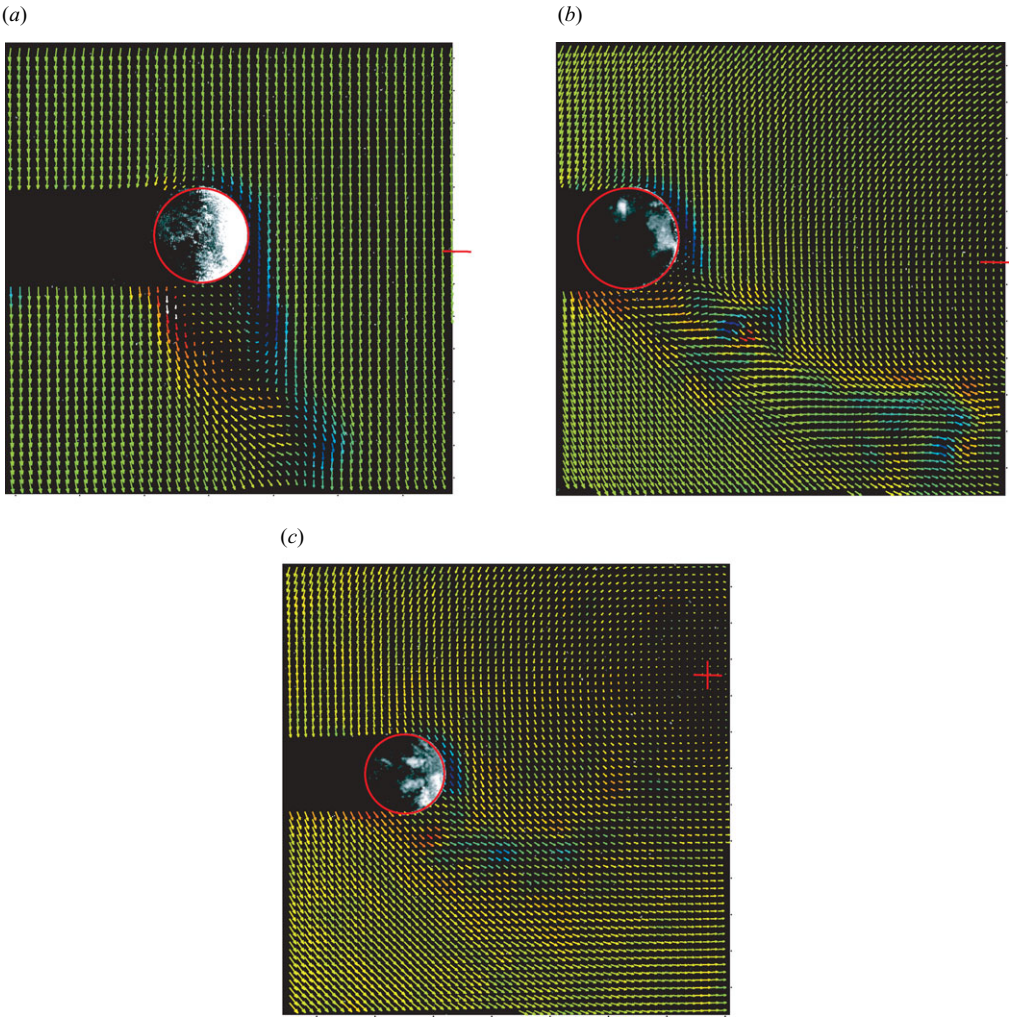

FIGURE 8. Flow field (indicated by arrows) and vorticity (indicated by colour, with green representing background vorticity). The sphere surface is indicated with a red circle. The high-fluid-velocity side is on the left side of the sphere. (*a*) The red line indicates the vertical position of the cylinder axis; the axis is out of sight. The sphere radius R is 3 mm; the cylinder rotation frequency ω is 0.2 Hz; $Re \approx 900$ and $Sr_\omega \approx 0.05$. The vortex shedding frequency is about 4 Hz. (*b*) $R = 4$ mm, $\omega = 0.5$ Hz, $Re \approx 600$, $Sr_\omega \approx 0.33$. The vortex shedding frequency is about 3.8 Hz. (*c*) The red cross indicates the cylinder axis; $R = 3$ mm, $\omega = 1.0$ Hz, $Re \approx 360$, $Sr_\omega \approx 0.67$. The vortex shedding frequency could not be determined.

in § 3.3 is much more pronounced than the motion along the cylinder axis, we may expect that the centres of the vortices remain mainly in one xy-plane.

In figure 9 the shedding process can be seen in more detail. We see the first image reproduced in the 14th, indicating that the shedding process has a frequency of about 4 Hz.

An interesting aspect of figures 8(*a*)–8(*c*) is the deflection of the wake which may return to the sphere as it is convected by the rotation of the liquid, as sketched in figure 10(*a*). This may occur if the wake has not diffused completely after one rotation or is not deflected sufficiently towards the cylinder axis. There might be

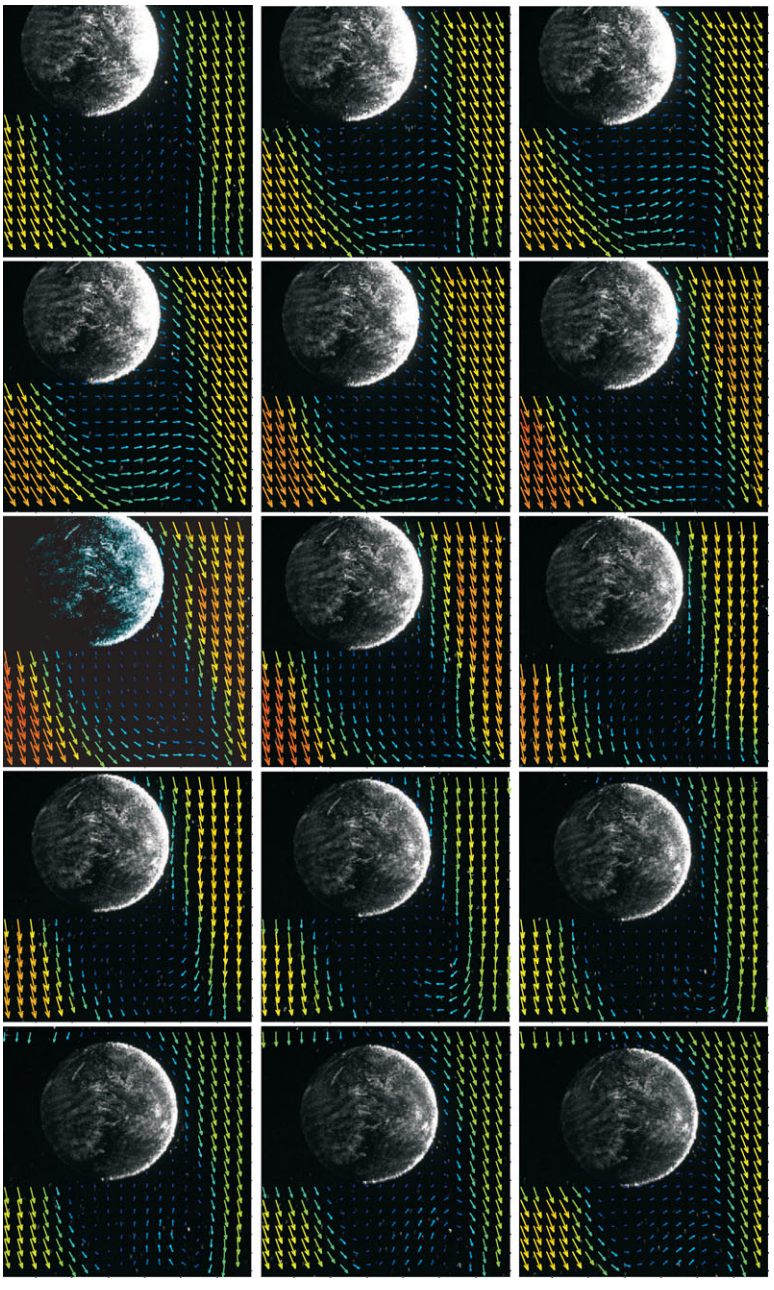

FIGURE 9. Sequence of PIV images for an LDPE sphere of 6 mm diameter with $f_c = 0.2$ Hz. The images are ordered in horizontal lines. The arrows indicate the flow field, and the colour of the arrows is a measure of the magnitude of the velocity. From the second to the last image one cycle is completed, and consecutive frames are 0.02 s apart. The vortex shedding frequency is about 4 Hz.

some similarity with a sphere located in the wake of another sphere upstream of it as indicated at the right side of figure 10(*a*).

We address first the wake diffusion and estimate for which set of parameters the wake length is such that it can interact with the sphere in the next revolution. The

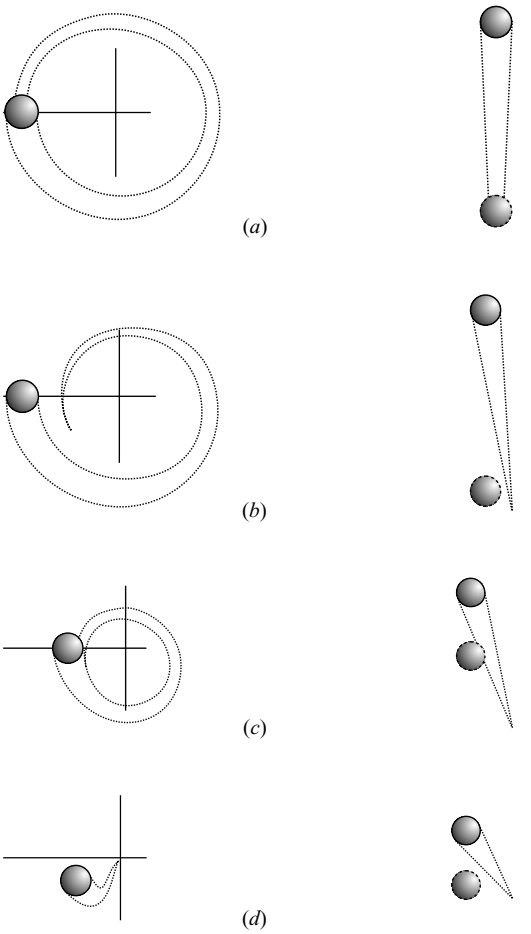

FIGURE 10. Left: sketch of the wake (between the dotted lines) behind the sphere. (*a*) The trajectory of the wake for the hypothetical case in which no deflection of the wake occurs. Particle equilibrium position (*b*) far from the cylinder axis, (*c*) at intermediate distance and (*d*) close to the cylinder axis. The crossing of the solid lines denotes the cylinder axis. Right: wake interaction of the sphere with the wake generated one period before. The polar angle is projected on a vertical line. The top particle represents the moment of wake generation. The bottom (dashed line) particle represents the moment at which this wake reaches the sphere.

velocity defect v_s along the wake axis in a uniform flow is (Landau & Lifshitz 1987, p. 70)

$$v_s = \frac{F_D}{4\pi\rho\nu s}, \tag{3.11}$$

where s is the coordinate along the wake and F_D is the drag force. After a full rotation $s = 2\pi r_e$, and for wake interaction to be negligible the velocity defect should be much less than the velocity of the undisturbed incident flow ωr_e. This holds when

$$\frac{C_D}{16\pi}\frac{R^2\omega}{\nu} \ll 1. \tag{3.12}$$

As a result we may expect wake interaction due to the rotation of the fluid when

$$Ta > \frac{32\pi}{C_D}. \tag{3.13}$$

For the last three liquids in table 1 $Ta \approx 50$ for most rotation rates, and thus wake interaction as indicated in figure 10(a) may be present.

Although the wake may survive a full cylinder revolution, it will not necessarily impinge on the sphere. From the momentum equation in the radial direction ($\partial p/\partial r = \rho u_\theta{}^2/r$, with p the pressure and r and θ the radial and angular directions) we see that for a given pressure gradient, the trajectory of the retarded fluid in the wake adopts a smaller radius. As a result the wake is deflected towards the cylinder axis. On the left side of figure 10 sketches of this deflection for different sphere positions are shown. For a sphere far away from the cylinder axis as in figure 8(a) (and sketched in figure 10b), the Reynolds number is high and the wake is long, but it will not interact with the sphere after a full rotation. In figure 8(b) (sketched in figure 10c) there may be interaction with the sphere. For even higher rotation rates, figure 8(c) (sketched in figure 10d) shows that the wake is strongly deflected towards the axis of the cylinder.

At the right side of figure 10 the effect of the wake on the sphere in the next revolution is sketched. Case (a) is hypothetical: the wake survives a full rotation and is not deflected at all. As a result the sphere feels its own wake as if it were the wake of an upstream sphere. In case (b) the wake also survives a full revolution but now is deflected. As a result the sphere will not feel its own wake. For a higher cylinder frequency as in (c) the wake is also deflected. The wake is shorter because the particle Reynolds number is lower at higher rotation frequencies. However, the path over which the wake may decay is also shorter. It is as if the two spheres in the representations at the right side of figure 10 were closer. In this case interaction occurs. For the last situation the deflection is too strong for interaction. It is difficult to formulate quantitative criteria for the transition among the different regimes. The above discussion serves merely to indicate possible wake-interaction scenarios, relevant for the interpretation of the data in the next sections.

3.5. *Results: dependence of lift and drag on the governing parameters*

This section discusses the dependence of the equilibrium position (r_e, ϕ_e), the drag and lift coefficients and the normalized particle spin rate on the governing parameters in terms of the dimensionless groups defined in (3.1). In the figures in this and the next section, results for the different liquids can be recognized by the symbols in the last column of table 1. In particular, the low-viscosity fluids are identified by ⋆ (liquid 8) and ◀ and ◁ (liquid 9).

Figure 11 shows the dependence of the equilibrium position of the particle on the Taylor number Ta. For each liquid the viscosity is constant, and an increase in Ta indicates a higher rotation frequency of the cylinder. As the cylinder rotation rate increases, the radial distance of the particle decreases, and the particle finds its equilibrium closer to the cylinder axis (figure 11a). The equilibrium angle ϕ_e is very close to π for $Ta < 1$ (i.e. for the more viscous fluid mixtures). For liquids 6–9 we see an increase with Ta at first, and as Ta increases further, the angle shows a sharp decrease for all liquids. However, the peaks for the different liquids do not occur at the same value of Ta.

From (3.7) and (3.8) we see that r_e and ϕ_e are related to the lift and drag coefficients. Therefore we inspect in figure 12 the effect of Ta on the lift and drag coefficients, as well as on the particle spin rate. The drag coefficient decreases when the viscosity

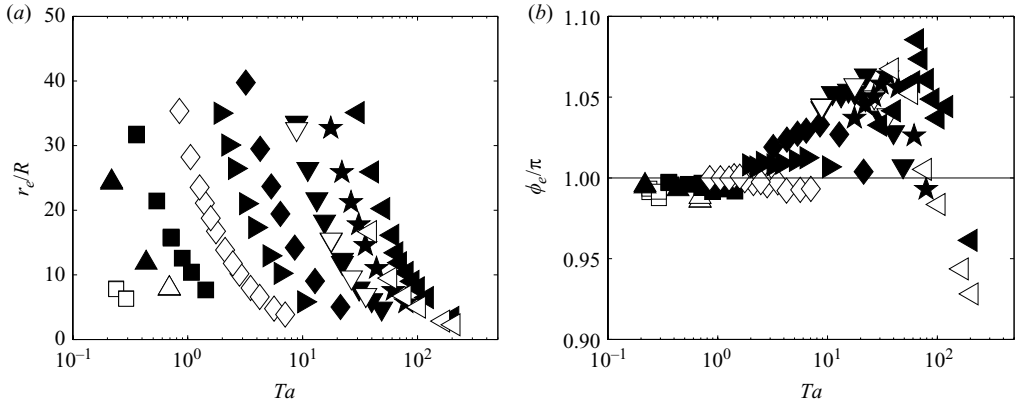

FIGURE 11. (*a*) Normalized radial distance of the particle centre and (*b*) angle with respect to the horizontal as a function of Ta (where ω is the primary control variable). The symbols are defined in table 1.

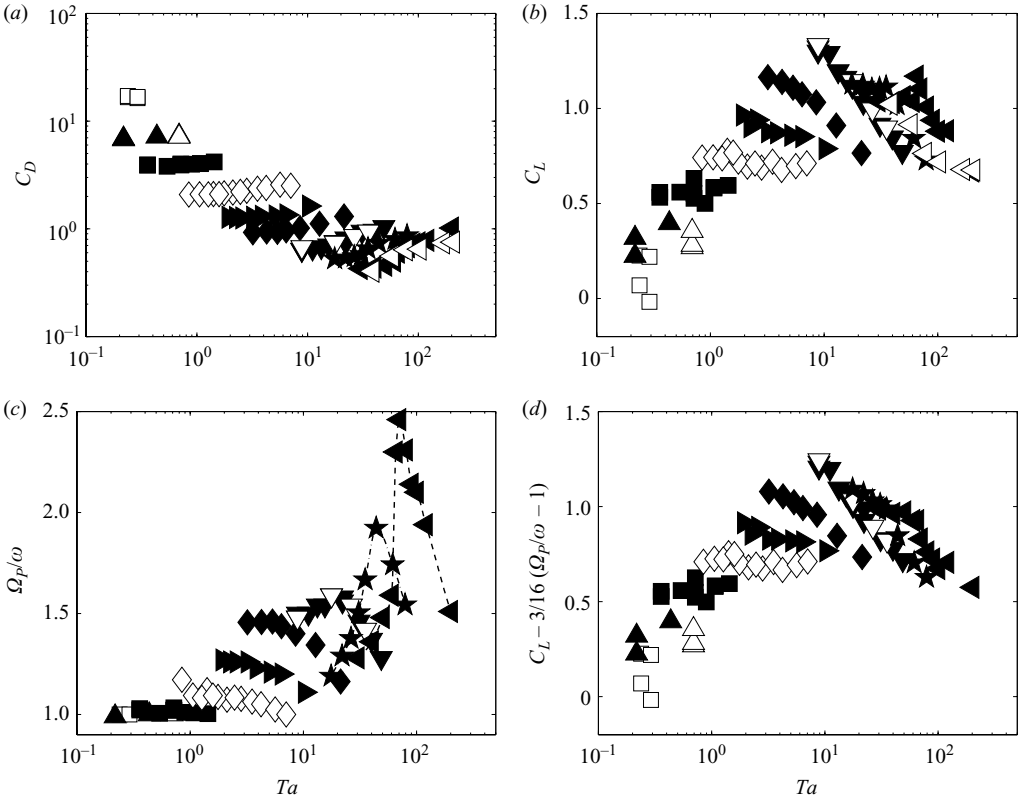

FIGURE 12. (*a*) Drag coefficient, (*b*) lift coefficient, (*c*) normalized particle spin rate and (*d*) lift coefficient corrected for spin as a function of Ta. The correction of the lift coefficient in (*d*) as compared with (*b*) is most prominent for liquids 8 and 9 (stars and triangles pointing left). The dashed (through the data of liquid 9) and dash-dotted (liquid 8) lines in (*c*) are to guide the eye.

of the liquid decreases (figure 12*a*). Each liquid data set shows a spread over a large range of Ta and a relatively small range of C_D. The lift coefficient and the normalized particle spin rate as a function of Ta are respectively shown in figures 12(*a*) and 12(*c*). The normalized particle spin rate shows peaks for liquids 7–9. A relatively small normalized sphere spin rate is observed when Ta (and consequently the cylinder rotation rate) is small for these liquids. The particle is then located far away from the cylinder axis. As the cylinder rotation rate increases and the particle equilibrium position is located closer to the axis, the spin rate increases. It then decreases for even higher cylinder rotation rates. This behaviour may be a consequence of the scenarios described in the previous section and sketched in figure 10. For sufficiently low Ta the ratio in (3.12) is small. The particle finds its equilibrium far from the cylinder axis. The wake can diffuse over a long trajectory before it reaches the particle again after one rotation and will not interact with the particle. As Ta increases, the particle equilibrium position is located more towards the cylinder axis. Now the sphere may interact with the wake as shown at the right side of figure 10(*c*). One side of the particle is in the wake, and the other is in the undisturbed flow. As a result a large torque acts on the sphere. Since the particle reaches a torque-free state, the spin rate will be very high under these circumstances. As Ta increases further and the particle is located even closer to the cylinder axis, the wake deflection may be so strong that the particle cannot interact with its wake (figure 10*d*). As mentioned before, for spheres very close to the cylinder axis we can expect the incident flow to be strongly disturbed by the particle.

A high spin rate of the sphere affects the measured lift coefficient. We define an excess spin as

$$\Omega_P/\omega - 1, \tag{3.14}$$

since for Stokes flow the normalized spin rate Ω_P/ω is 1. In figure 12(*d*) the lift coefficient is corrected for the particle spin, assuming that the extra part of the lift coefficient that is due to the spin is given by (2.14). By subtracting the part of the lift coefficient that is due to excess spin we find the corrected lift coefficient $C_L - (3/16)(\Omega_P/\omega - 1)$. The effect on the lift due to the spin has only been demonstrated for $5 \leqslant Re \leqslant 200$. However, we apply (2.14) to the complete experimental data range and evaluate the resulting lift coefficient when the part that is due to the excess spin is subtracted. In figure 12(*d*) we see that the deviation of the highest values of the lift coefficient is smaller after correcting it for the high spin rates, in particular in liquid 9.

Figure 13 shows the dependence of the equilibrium position of the particle on the Galilei number Ga defined in (3.1). For each liquid the Galilei number is a constant, and the figure shows the spread of r_e and ϕ_e. The effect of Ga on the lift and drag coefficients and the particle spin rate is shown in figure 14. Figure 14(*a*) shows a decrease of the drag coefficient with Ga. Since the Galilei number is based on the terminal rise velocity which is close to the undisturbed velocity in Re (which is a result of a balance mainly between drag and buoyancy forces), this is according to expectation. The lift coefficient in figure 14(*b*) shows an increasing trend with Ga up to $Ga \approx 206$. After that C_L decreases. The highest lift coefficients in liquids 8 and 9 are smaller than in liquid 7. According to Jenny *et al.* (2004) we may expect the critical Galilei number for which the particle trajectory becomes unstable to be between 175 and 180 for our density ratios ($\rho_p/\rho \approx 0.9$). The particles in liquids 1–6 should all have axisymmetric wakes at the same Galilei number in a uniform flow. Liquid 7 ($Ga \approx 206$) is in the periodic zigzagging regime. Liquids 8 and 9 are in the three-dimensional chaotic regime. The transition to an unsteady wake coincides with

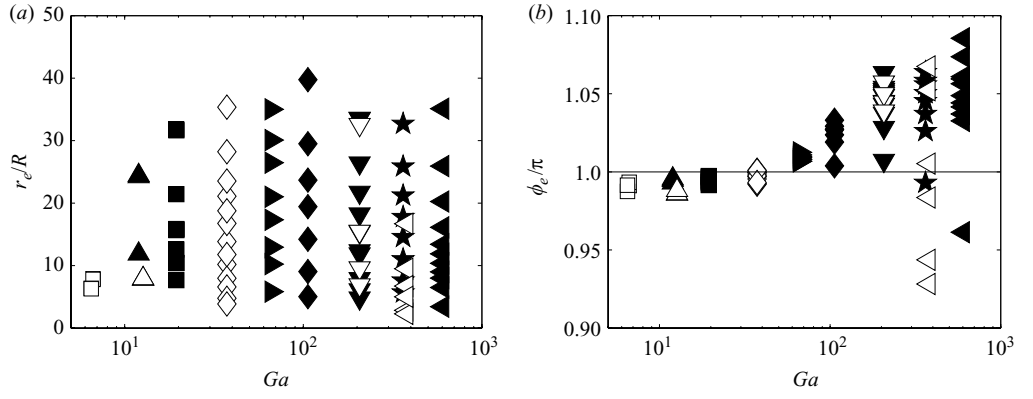

FIGURE 13. (*a*) Normalized radial distance of the particle centre and (*b*) angle with respect to the horizontal as a function of Ga.

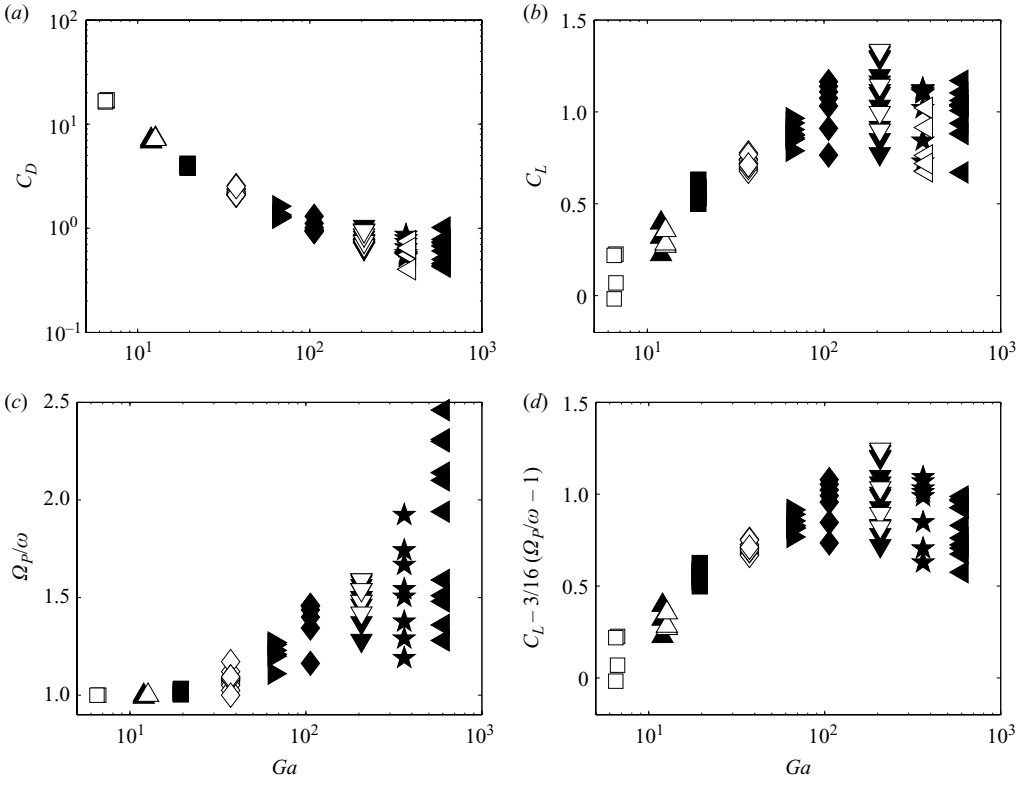

FIGURE 14. (*a*) Drag coefficient, (*b*) lift coefficient, (*c*) normalized particle spin rate and (*d*) lift coefficient corrected for spin as a function of Ga.

a decrease of the lift coefficient. Figure 14(*c*) indicates that the spread of the rotation rates in the same liquid increases with Ga. Whereas the envelope of the highest values of C_L shows an indentation for liquid 8 in figure 14(*b*), this is removed when correcting the lift coefficient for the excess particle spin (figure 14*d*).

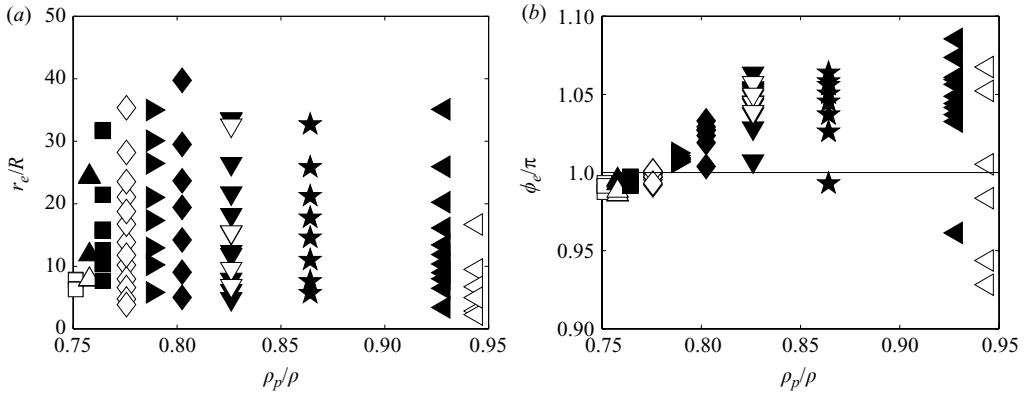

FIGURE 15. (*a*) Normalized radial distance of the particle centre and (*b*) angle with respect to the horizontal as a function of the density ratio ρ_p/ρ.

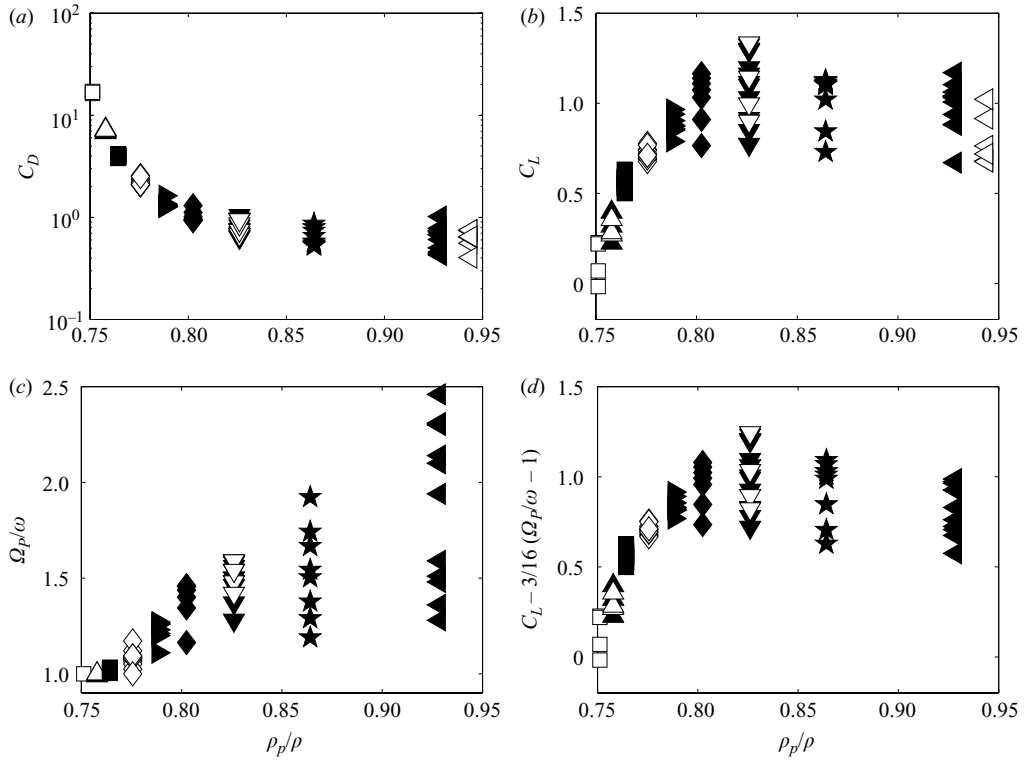

FIGURE 16. (*a*) Drag coefficient, (*b*) lift coefficient, (*c*) normalized particle spin rate and (*d*) lift coefficient corrected for spin as a function of the density ratio ρ_p/ρ.

In figures 15 and 16 the results are plotted as functions of the density ratio ρ_p/ρ. They show trends similar to those in figures 13 and 14. As the viscosity of the liquids in table 1 decreases, the density ratio increases towards one. For a density ratio larger than one, the equilibrium position is no longer stable; so we can expect that the equilibrium positions become less stable for the less viscous liquids.

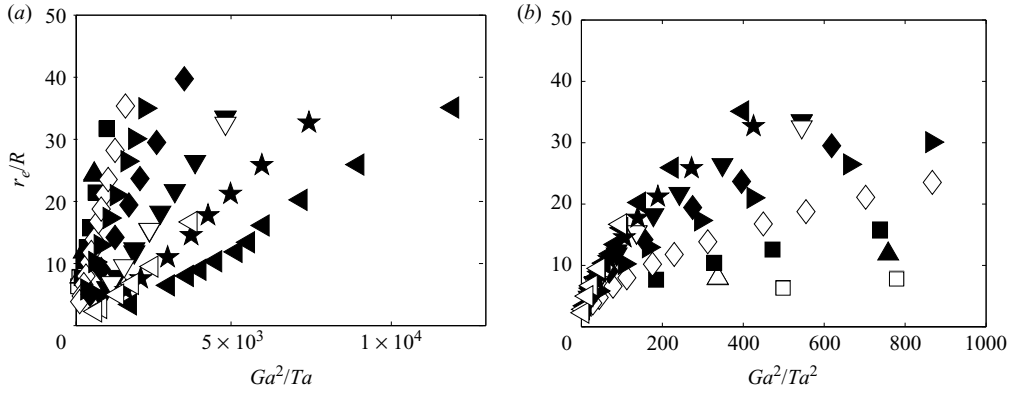

FIGURE 17. Normalized radial distance of the particle centre as a function of (*a*) Ga^2/Ta and (*b*) Ga^2/Ta^2.

The effect on the particle trajectories can be seen in figures 4–7, where, generally speaking, the excursions around the equilibrium position are larger in liquids of lower viscosity. Figure 16 shows the trend of the lift and drag coefficient as a function of the density ratio. For each liquid both the density ratio and the Galilei number vary. The behaviour shown in the figure can thus be a result of a different Galilei number instead of a different density ratio. In fact, the data for the smaller sphere in liquid 9 (◁) fall in the same range of values of C_D and C_L as the data in liquid 8 (⋆). The two liquids correspond to a different value for the density ratio but the same Galilei number. Thus the Galilei number is a more appropriate parameter to describe the results. Apparently, the viscosity is important to describe the drag and lift trends.

The representation of the equilibrium position, drag and lift coefficient and spin rate in terms of Ga, Ta and ρ_p/ρ has not revealed simple relationships. Comparing the results in this section, the equilibrium angle ϕ_e is best described by the Taylor number as in figure 11. As suggested in § 3.1, r_e/R may be best described by a combination of Ga and Ta. In figure 17 we have plotted r_e/R versus Ga^2/Ta and Ga^2/Ta^2. Figure 17(*a*) yields the best results for the viscous fluids, as was predicted by (3.5).

3.6. *Results: dependence of lift and drag on other parameters*

In figures 14(*a*) and 16(*a*) we found some collapse of the drag coefficient on to a curve for the Galilei number and the density ratio. The lift coefficient and the sphere spin rate cannot be represented as functions of one of the parameters Ta, Ga and ρ_p/ρ alone. In this section we will study the effects of other dimensionless numbers on drag, lift and particle spin. We include in our analysis the measured r_e/R of the system, which is a function of Ta, Ga and ρ_p/ρ. The equilibrium position appears in the definition of the Reynolds number Re, the Froude number Fr (3.9) and the dimensionless vorticity Sr_ω (3.10). The dimensionless vorticity is the normalized velocity difference over the sphere and therefore resembles a dimensionless shear rate. Since in the literature lift and drag coefficients are frequently represented as functions of the Reynolds number and the dimensionless shear rate these are obvious choices. The Froude number expresses the relative importance of the centripetal acceleration with the gravitational acceleration and has been indicated as a relevant parameter

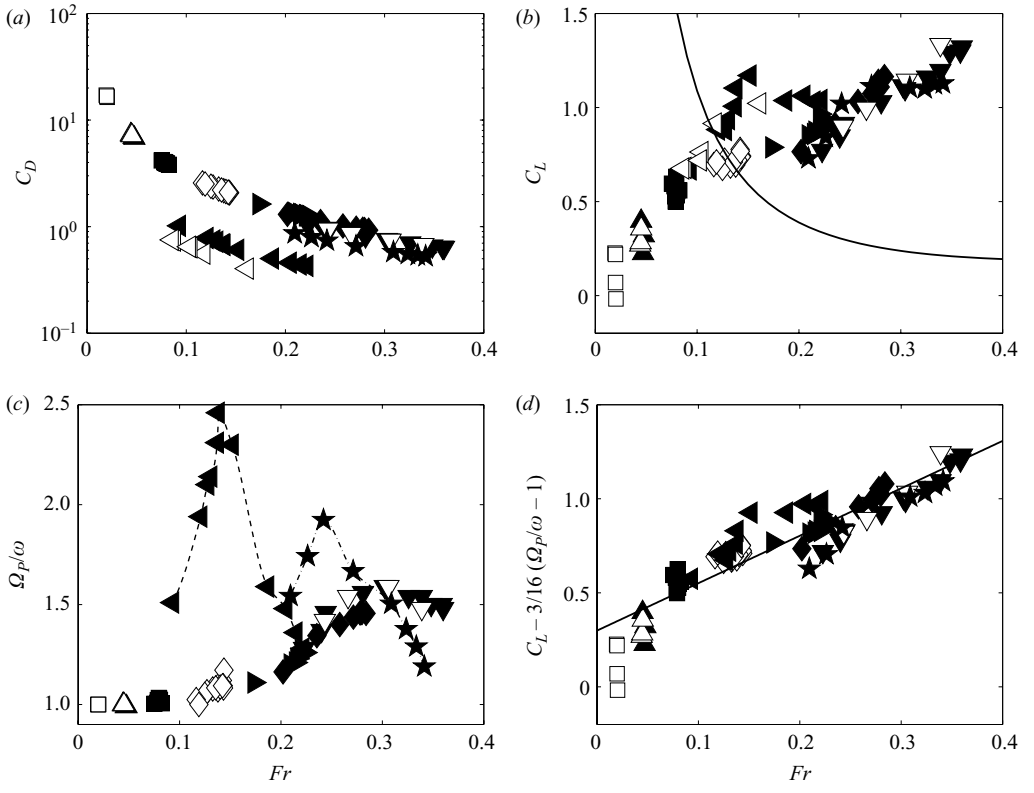

FIGURE 18. Drag coefficient, lift coefficient and normalized particle spin rate as a function of Fr. The solid line in figure 18(b) is the parameterization of the lift coefficient for bubbles according to Naciri (1992): $C_L^N = (1/2)(1 + C_A) - 0.81/\sqrt{Fr} + 0.29/Fr$. The solid line in figure 18(d) is a fit to the corrected lift coefficient data (3.15).

by Naciri (1992) for a bubble in a horizontally rotating system. We will therefore also study the effect of Fr on the lift and drag coefficients and the particle spin.

The effect of Fr is shown in figure 18. The drag coefficients collapse on to one curve, except those of liquids 8 and 9 (figure 18a). The lift coefficients in figure 18(b) are compared with the parameterization for bubbles by Naciri (1992). Clearly, his parameterization is not valid for solid spheres. The particle spin cannot be represented as a function of Fr (figure 18c). However, we can correlate the high spin rates to the peaks in the lift coefficient. Subtracting the contribution to the Magnus-like lift (2.14) owing to the excess spin yields the corrected lift coefficient (figure 18d). The data are fitted as a linear function of Fr,

$$C_L - \frac{3}{16}\left(\frac{\Omega_P}{\omega} - 1\right) = 2.52\,Fr + 0.30. \tag{3.15}$$

This fit describes the dependence of C_L on Fr for most data reasonably well. Again we find that the correction of the lift that is due to excess particle spin improves the collapse of the data on to a single curve.

We now consider the dependence on the Reynolds number and the vorticity parameter. For the first three liquids in table 1 the Reynolds number is more or less constant. This is a direct result of substituting (3.5) in the definition of the Reynolds

number (3.9) and remembering that the viscosity and particle radius are constant in each liquid. For fluids with a low viscosity the radial distance decreases with the square of the cylinder rotation rate (3.6), and thus the Reynolds number is modified by varying the rotation rate of the cylinder. As a result, both the Reynolds number and the vorticity parameter depend on the cylinder rotation rate for the less viscous fluids and cannot be varied independently. From linear shear flow results we know that the shear rate has an effect on drag and lift. We may expect similar behaviour for our vorticity parameter. Moreover, the vorticity parameter indicates the proximity of the sphere to the cylinder axis. As indicated in § 3.4 the distance between the sphere and the cylinder axis affects the wake-interaction behaviour. In an attempt to study the effects of both the Reynolds number and the dimensionless vorticity simultaneously, we plot the results as a function of the Reynolds number, indicating the vorticity parameter by a colour in figure 19.

In figures 19 and 20 the experimental and numerical data are compared. The numerical data points from figure 2 are represented by (blue) circles. Figure 19 displays all experimental data, whereas in figure 20 only data points for which $Sr_\omega \leqslant 0.1$ are shown. This allows an adequate comparison between numerical and experimental results, since for the numerical results $Sr_\omega = 0.1$.

In figures 19(a) and 20(a) the experimentally determined drag coefficients are compared with the standard drag curve and the numerical data. It is clear from figure 19(a) that as the vorticity parameter increases, the drag coefficient generally increases. For the experimental data with $Sr_\omega \leqslant 0.1$ there is an excellent agreement of the experimental data with the standard drag curve, as shown in figure 20(a).

Figures 19(b) and 20(b) show the lift coefficient. The solid line represents the fit to the numerical data (2.15). Figure 20(b) shows that the experimental data with $Sr_\omega \leqslant 0.1$ and $Re < 200$ fall on to (2.15), apart from the data around $Re = 5$. As indicated in table 1 the measurement uncertainty of C_L is high at $Re = 5$. Figure 19(b) indicates that an increase in Sr_ω generally results in a decrease in C_L. Up to liquid 7 (▼, ▽) C_L increases; in liquids 8 and 9 the values of C_L decrease. Figure 19(b) shows a small increase in C_L for liquid 9 (◀, ◁) with respect to liquid 8 (⋆). In this liquid we observe high sphere spin rates and thus can expect a strong Magnus-like effect, increasing C_L. When we correct the C_L for excess spin as described in § 3.5 we find the results indicated in figures 19(d) and 20(d). Now the decrease of the corrected lift coefficient for higher Reynolds numbers is smooth. It is of course not clear whether it is valid to assume the same effect of particle spin on the lift coefficient as in (2.14) in this Reynolds range, since we have no numerical data to validate this. However, these corrected results indicate a trend in the lift coefficient that is well worth exploring.

In figures 19(b)–19(e) and 20(b)–20(d) the dotted line at $Re = 212$ indicates the transition in a uniform flow where the wake becomes non-axisymmetric. The dash-dotted line at $Re = 274$ indicates the transition where the wake becomes unsteady. The dashed lines in figures 20(b) and 20(d) are the fits through the average values of Re and C_L in liquids 7–9. The number of data points used to determine these fits is of course insufficient to allow more than an indication of a trend. However, it is interesting to see where this trend crosses the numerical fit (2.15) for $Re \leqslant 200$. In figure 20(b) the crossover is close to $Re = 212$ (the Reynolds number at which in a uniform flow the wake loses its axisymmetry); in figure 20(d) it is close to $Re = 274$ (the Reynolds number at which in a uniform flow the wake becomes unsteady). Since $Sr_\omega \leqslant 0.1$ in this figure, we can expect perhaps a behaviour similar to that in a uniform flow. Observing the Reynolds number at which C_L starts to decrease, it is probable

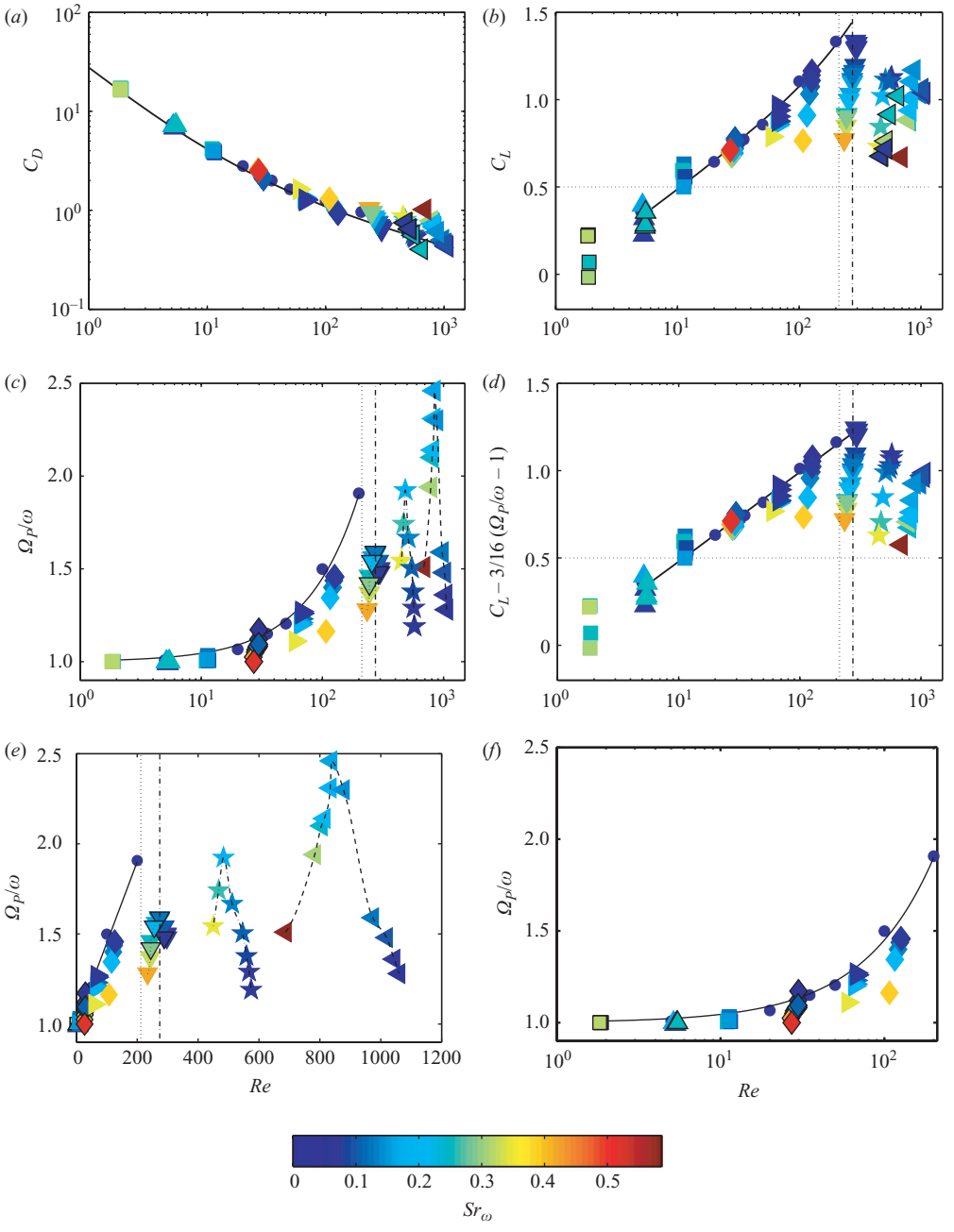

FIGURE 19. Drag coefficient, lift coefficient and normalized particle spin rate as a function of Re. The spheres represent the numerical results. The solid line in (a) represents the standard drag curve. The solid line in (b) represents the fit to the numerical data of the lift coefficient (2.15). The solid lines in (c), (e) and (f) represent the fit to the normalized spin rates from the numerical data (2.13). The solid line in (d) represents the fit to the numerical data of the lift coefficient (2.15) with 3/16 (0.0045 Re) subtracted. The vertical dotted line at $Re = 212$ marks the transition to a non-axisymmetric wake, and the vertical dash-dotted line at $Re = 274$ denotes the transition to a unsteady wake, both in case of a uniform flow. The other lines function again as guides to the eye.

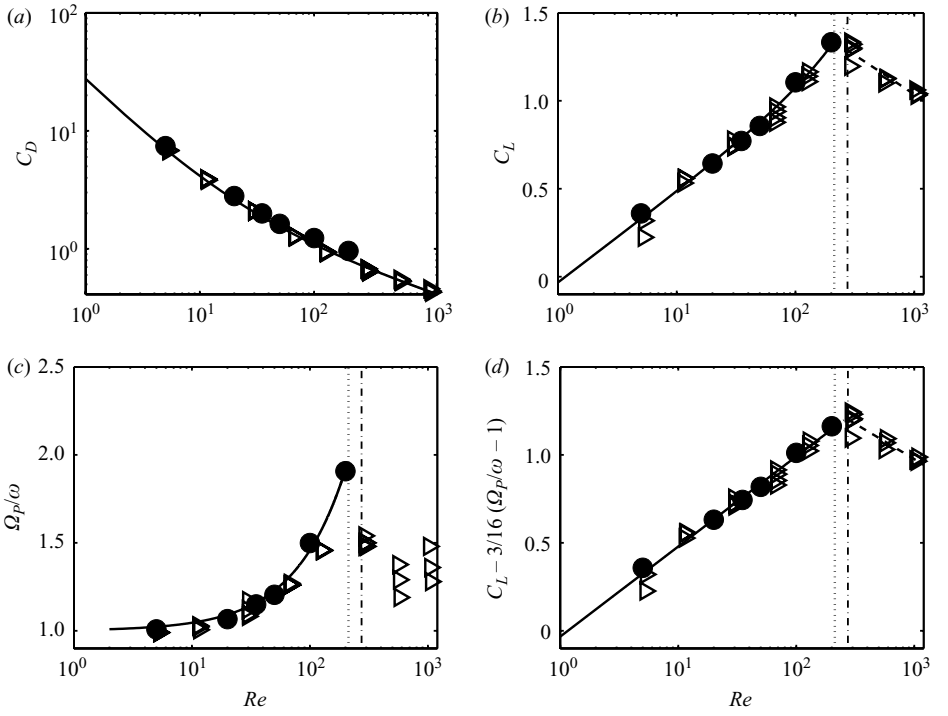

FIGURE 20. Drag coefficient, lift coefficient and normalized particle spin rate as a function of Re, for $Sr_\omega \leqslant 0.1$. The circles are numerical data, and the open triangles are experimental data. The solid line in (*a*) represents the standard drag curve. The solid line in (*b*) represents the fit to the numerical data of the lift coefficient (2.15) for $Re < 200$. The dashed line is a fit to the average values per liquid: $C_L = -0.45\ \log_{10} Re + 2.37$ for $Re > 212$. The solid line in (*c*) represents the fit to the normalized spin rates from the numerical data (2.13). The solid line in (*d*) represents the fit to the numerical data of the lift coefficient (2.15) with 3/16 (0.0045 Re) subtracted. The dashed line is again a fit to the average values per liquid: $C_L - 3/16\ (\Omega_P/\omega - 1) = -0.40\ \log_{10} Re + 2.18$ for $Re > 274$. The vertical lines are as in figure 19.

that some change in the wake structure of the sphere causes the decrease of C_L (see also the discussion of C_L as a function of Ga in § 3.5).

Figures 19(*f*) and 20(*c*) compare the experimentally observed sphere spin ratio (Ω_P/ω) to the numerical data and show again good agreement for $5 \leqslant Re \leqslant 127$ and $Sr_\omega \leqslant 0.1$. The solid lines in these figures represent the fit to the numerical data (2.13). The experimental data follow the fit well up to liquid 6. The data in liquid 7 show a sudden decrease compared to the numerical trend (figures 19*c*, 19*e* and 20*c*). Since these data are beyond the Reynolds numbers at which the transitions in the wake in a uniform flow occur, the decrease in Ω_P/ω may be a consequence of changes in the wake structure behind the sphere as well.

For liquids 7–9 the experimental data show effects that are not seen in the lower Reynolds range: for high Sr_ω, Ω_P/ω is low, followed by a peak in each liquid as the Sr_ω decreases, after which Ω_P/ω decreases (figure 19*e*). In figure 21 the spin rate is plotted as a function of the vorticity parameter (indicating the distance to the cylinder axis). For liquid 7 the peak in the spin rate is around $Sr_\omega = 0.13$, $Re = 274$. For liquids 8 and 9 the peak is around $Sr_\omega = 0.18$. For the last two liquids wake interaction

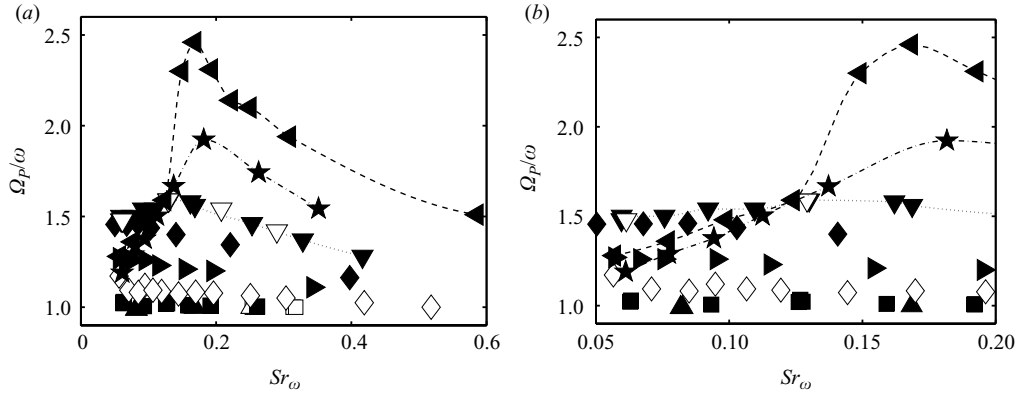

FIGURE 21. Normalized particle spin rate as a function of the vorticity parameter. Enlarged plot on the right-hand side.

(as described in the scenarios in § 3.4 and sketched in figure 10) is considered to be the cause of the high Ω_P/ω data points. The interaction depends on the wake length and the proximity to the cylinder axis and thus on Re and Sr_ω. For liquid 7, the peak occurs for lower Sr_ω. Here, instead of wake interaction, wake instability may be the cause of the decrease in Ω_P/ω. The initial increase of Ω_P/ω may be because of the increase in the Reynolds number. The spin rate then decreases when the wake behind the particle becomes unsteady. This is supported by the value of Re at which the decrease in Ω_P/ω occurs ($Re = 274$, where in a uniform flow the wake becomes unsteady) as well as by the relatively moderate decrease in Ω_P/ω compared with that in liquids 8 and 9. The particle spin rates in figure 20(c) show a large spread for liquids 8 and 9 even though $Sr_\omega \leqslant 0.1$. It appears that Sr_ω is a much more relevant parameter to describe the sphere spin than Re for the liquids in the range $Re > 200$.

To evaluate the effect of the vorticity parameter Sr_ω on the data we normalize each data point by the value we find at the same Re and for no Sr_ω (in the case of the drag coefficient) or small Sr_ω (in the case of the lift coefficient). For the drag, we do this by normalizing the drag coefficients by the value of the standard drag curve at the corresponding Reynolds number. Figure 22(a) shows the result for liquids 1–6 plotted versus Sr_ω. It also shows an error estimate. Because it contains the error not only in the drag coefficient but also in the Reynolds number, the error bars are rather large. The overall trend shows a linear increase of $C_D/C_{D,standard}$ with Sr_ω. Figure 22(b) shows the normalized drag coefficient for the data in liquids 7–9. Again $C_D/C_{D,standard}$ increases with Sr_ω; however for liquids 8 and 9 there is a sudden strong increase in the normalized drag coefficient around $Sr_\omega = 0.15$. Comparing figure 22(b) with figure 21 shows that this rise occurs for the data for which the particle spin is strongly enhanced. As discussed above this is due to wake interaction which changes the incident flow; thus, we are considering data here with a disturbed incident velocity. However, the wake interacting with the sphere is expected to result in a decreased drag (a shielding effect). Therefore the increase of the drag coefficient cannot be the result of the disturbance of the flow field but is a result of the increase of the sphere spin. Moreover, the rise in the drag coefficient is strongest for liquid 9, where also the spin rates rise strongest. The linear shear flow results of Bagchi & Balachandar (2002a) show that in their case the drag is not significantly influenced by the sphere spin. However the spin of the sphere normalized by the rotation of the flow is always below one in the case of a linear shear flow. We find values of Ω_P/ω around 2.5 for

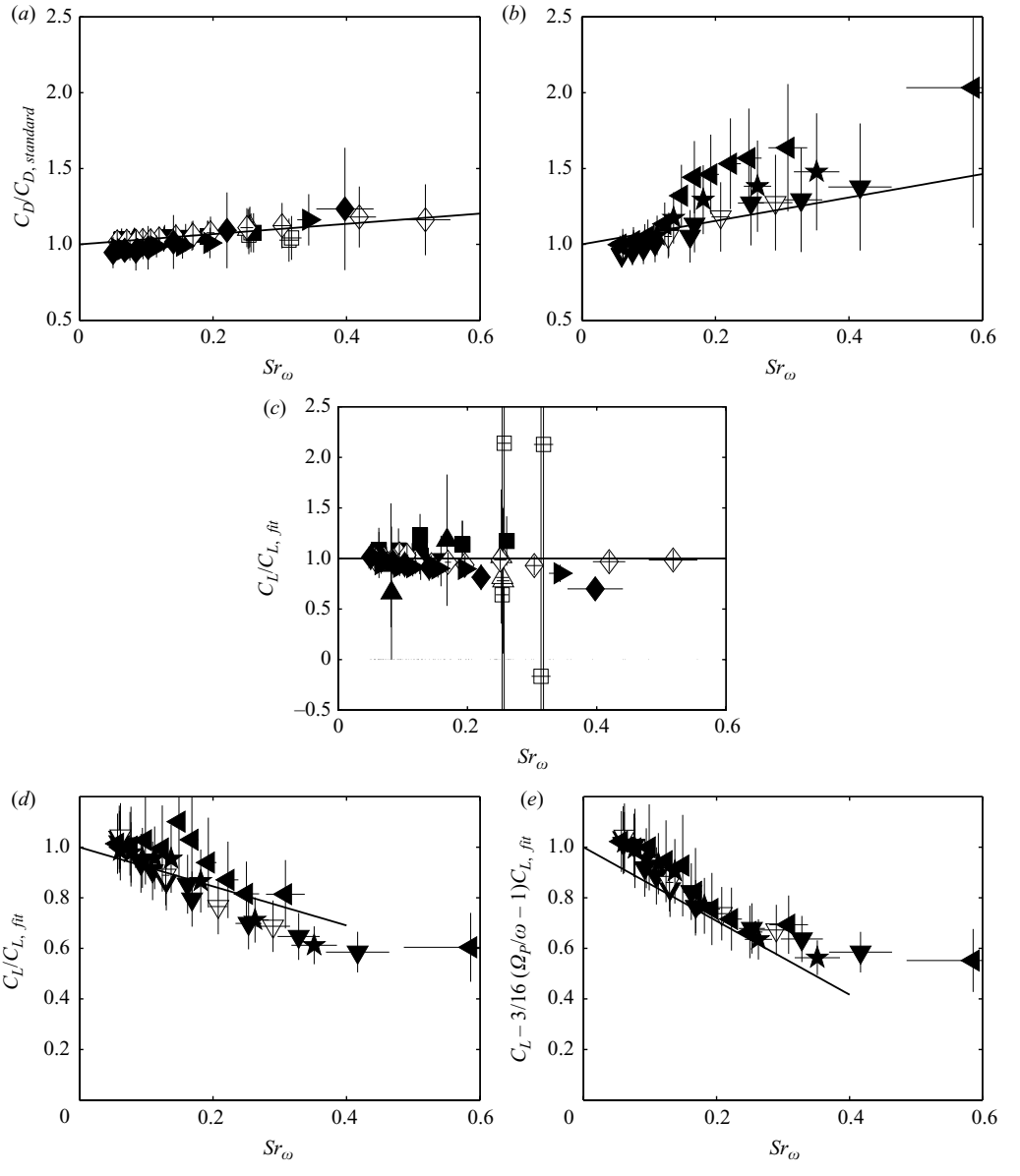

FIGURE 22. Drag coefficient normalized by the standard drag coefficient and lift coefficient normalized by (2.15) in (*c*) and by the fits from figures 20(*b*) and 20(*d*) through the average values of data with $Sr_\omega \leqslant 0.1$ and $Re \geqslant 200$ in (*d*) and (*e*). For (*a*) and (*c*) $Re < 130$; for (*b*), (*d*) and (*e*) $Re > 200$. The solid lines are the fits to the data. In (*a*), $C_D/C_{D,standard} = 0.34Sr_\omega + 1$; in (*b*), $C_D/C_{D,standard} = 0.77Sr_\omega + 1$. In (*d*), $C_L/C_{L,fit} = -0.77Sr_\omega + 1$; in (*e*), $(C_L - 3/16(\Omega_P/\omega - 1))/C_{L,fit} = -1.46Sr_\omega + 1$.

liquid 9 and around 2 for liquid 8. Apparently, such high particle spin rates affect the drag coefficient. After the steep increase in drag coefficient, C_D appears to rise linearly with Sr_ω; however the data of different liquids no longer collapse on to the same line. Figure 21 shows that for the higher values of Sr_ω, liquid 9 displays higher values of particle spin. This may be the cause of the higher C_D values of liquid 9.

Figure 22(*c*) shows the lift coefficients normalized by the value of the lift coefficient for low Sr_ω obtained by fitting the numerical data (2.15) as a function of Sr_ω for $Re < 130$. No apparent effect of Sr_ω is clear from this figure. For the data with higher Reynolds numbers, we have no prediction of what the lift coefficient should be for low Sr_ω; however we can use the fit of the average of the experimental data with low Sr_ω and high Re (the dashed line in figure 20*b*) to normalize C_L. Figure 22(*d*) shows this normalized lift coefficient as a function of Sr_ω for $Re > 200$. In this range we see a clear trend: the lift coefficient decreases with the shear rate up to $Sr_\omega = 0.4$. After that the curve flattens. For liquid 9 we see an anomaly for the data that have high particle spin rates. The trend of the lift decreasing with Sr_ω is even more apparent if we study the lift coefficient, corrected by the particle spin (figure 22*e*). The corrected lift coefficients are now normalized by the fit through the average of the corrected lift coefficients with low Sr_ω and high Re (the dashed line in figure 20*d*). The anomaly has now disappeared, and the data collapse better on to one line.

4. Summary and conclusions

We experimentally obtained the drag and lift coefficients for a sphere in a solid-body rotating flow by measuring the equilibrium location of the sphere in the cylinder. The data span the range $0.1 < Re \leqslant 1060$. We compared these data to previously obtained numerical data in the range $5 < Re \leqslant 200$.

The Reynolds number, the vorticity parameter Sr_ω (3.10) and, for the experimental data, the Froude number, are all relevant dimensionless numbers for modelling the forces on a sphere in this type of flow.

For $Sr_\omega \leqslant 0.1$ and $5 < Re < 1060$ the experimental results for the drag coefficient show an excellent agreement with the standard drag curve. For higher shear rates the drag increases linearly with Sr_ω.

Regarding the lift coefficient several conclusions can be drawn:

(i) For $Sr_\omega = 0.1$ and $5 < Re < 200$ the results of the numerical simulations for non-rotating and freely rotating spheres suggest that the lift coefficient can be decoupled in a flow-induced part and a part that is due to the sphere spin (the Magnus-like lift).

(ii) Both numerical simulations and experiments indicate a logarithmic increase of the flow-induced lift coefficient with the Reynolds number for a freely rotating sphere in a solid-body rotating flow in the range $Sr_\omega \leqslant 0.1$ and $5 < Re < 200$. The vorticity parameter has no substantial effect on C_L if $Re < 130$. Contrary to the results for bubbles in Van Nierop *et al.* (2007) no negative lift coefficients were observed for a spinning sphere. The normalized particle spin rate rises linearly with Re and shows good agreement with the numerical data up to $Re \sim 130$ provided $Sr_\omega \leqslant 0.1$.

(iii) By introducing the Froude number it is possible to realize a collapse of the lift coefficients on to a straight line.

For Reynolds numbers above 200 the dynamics becomes different. The excursion of the sphere around its equilibrium position becomes larger. The experimentally determined drag coefficients still follow the standard drag curve for data with $Sr_\omega \leqslant 0.1$. However, the lift coefficient now decreases as a function of Re. It also decreases with Sr_ω, and the decrease is linear after the lift coefficients have been corrected for particle spin. The sphere spin rate for data with $Sr_\omega \leqslant 0.1$ no longer increases linearly with Re. The changes in the behaviour of the lift coefficient and the sphere spin rate are attributed to changes in the structure of the wake behind the sphere.

The three experimental liquids in the higher-Reynolds-number regime all display a peak in the spin rate. We ascribe this to the particle interacting with its own wake. PIV images have shown that the wake is bent towards the cylinder axis. If the particle is close to the axis, one side may be in the wake, and this will result in a high particle spin. As the particle moves away from the cylinder axis, there is no longer interaction with the wake, and the particle spin rate decreases. If the particle is very close to the axis the incident flow is completely disturbed, and the spin rate is lowered.

We would like to thank Jacques Magnaudet and Dominique Legendre for the use of their numerical code Jadim to validate our results and G. W. H. Bruggert and M. Bos for building the experimental set-up. This work is part of the research programmes of STW and FOM and is financially supported by NWO. The development of the Physalis code used in this work has been supported by the US National Science Foundation under grants CTS 0625138 and CBET 0754344 to A. Prosperetti.

Appendix A. Tabulated experimental values

Liquid no.	r_e (cm)	ϕ_e	ω (s^{-1})	R (mm)	ρ ($g\,cm^{-3}$)	C_D	C_L	Ω_P/ω
1.00	3.13	3.11	1.26	3.97	0.93	16.70	0.07	1.00
1.00	3.09	3.12	1.26	3.97	0.93	17.13	0.23	1.00
1.00	2.53	3.10	1.57	3.97	0.93	16.35	−0.02	1.00
1.00	2.50	3.11	1.57	3.97	0.93	16.76	0.22	1.00
2.00	9.62	3.12	0.63	3.97	0.93	6.88	0.22	0.99
2.00	9.70	3.13	0.63	3.97	0.93	6.77	0.32	0.99
2.00	4.71	3.12	1.26	3.97	0.93	7.17	0.40	1.00
2.00	3.11	3.10	1.88	3.97	0.93	7.31	0.27	1.00
2.00	3.13	3.10	1.88	3.97	0.93	7.23	0.28	1.00
2.00	3.14	3.10	1.88	3.97	0.93	7.15	0.36	1.00
3.00	12.56	3.13	0.63	3.97	0.93	3.93	0.53	1.03
3.00	12.61	3.13	0.63	3.97	0.93	3.90	0.56	1.02
3.00	6.22	3.12	1.26	3.97	0.93	4.00	0.53	1.02
3.00	6.26	3.13	1.26	3.97	0.93	3.95	0.63	1.03
3.00	6.30	3.12	1.26	3.97	0.93	3.91	0.55	1.02
3.00	4.13	3.12	1.88	3.97	0.93	4.04	0.58	1.01
3.00	4.13	3.12	1.88	3.97	0.93	4.03	0.58	1.01
3.00	3.04	3.12	2.51	3.97	0.93	4.18	0.60	1.00
3.00	8.51	3.13	0.94	3.97	0.93	3.81	0.56	1.01
3.00	4.99	3.11	1.57	3.97	0.93	3.98	0.50	1.01
4.00	8.37	3.14	1.26	3.97	0.93	2.10	0.78	1.12
4.00	5.50	3.13	1.88	3.97	0.93	2.17	0.69	1.07
4.00	4.04	3.13	2.51	3.97	0.93	2.25	0.69	1.08
4.00	3.17	3.13	3.14	3.97	0.93	2.36	0.72	1.06
4.00	2.62	3.12	3.77	3.97	0.93	2.39	0.68	1.05
4.00	1.89	3.12	5.03	3.97	0.93	2.57	0.70	1.02
4.00	14.03	3.14	0.75	3.97	0.93	2.08	0.74	1.17
4.00	11.20	3.14	0.94	3.97	0.93	2.09	0.74	1.09
4.00	9.34	3.14	1.13	3.97	0.93	2.09	0.74	1.08
4.00	6.65	3.14	1.57	3.97	0.93	2.14	0.72	1.09
4.00	4.67	3.13	2.20	3.97	0.93	2.21	0.71	1.08
4.00	7.45	3.14	1.41	3.97	0.93	2.10	0.77	1.09

TABLE 2. Values of the experimental input parameters (liquid, ω, R, ρ), output parameters (r_e, ϕ_e, x_e, y_e, Ω_P/ω) and calculated values of C_D and C_L.

Liquid no.	r_e (cm)	ϕ_e (s^{-1})	ω (mm)	R ($g\,cm^{-3}$)	ρ	C_D	C_L	Ω_P/ω
4.00	1.53	3.12	6.28	3.97	0.93	2.51	0.71	1.00
5.00	10.50	3.17	1.26	3.97	0.93	1.26	0.94	1.26
5.00	6.88	3.17	1.88	3.97	0.93	1.31	0.87	1.23
5.00	5.14	3.18	2.51	3.97	0.93	1.32	0.86	1.21
5.00	4.06	3.18	3.14	3.97	0.93	1.35	0.85	1.20
5.00	2.31	3.16	5.03	3.97	0.93	1.63	0.79	1.11
5.00	13.89	3.17	0.94	3.97	0.93	1.28	0.97	1.27
5.00	8.34	3.17	1.57	3.97	0.93	1.28	0.88	1.26
5.00	11.94	3.16	1.10	3.97	0.93	1.27	0.90	1.26
6.00	11.71	3.22	1.26	3.97	0.93	0.94	1.14	1.46
6.00	7.71	3.23	1.88	3.97	0.93	0.97	1.07	1.44
6.00	5.64	3.25	2.51	3.97	0.93	1.02	1.03	1.40
6.00	3.59	3.23	3.77	3.97	0.93	1.11	0.91	1.34
6.00	15.78	3.20	0.94	3.97	0.93	0.93	1.16	1.46
6.00	9.40	3.23	1.57	3.97	0.93	0.94	1.11	1.46
6.00	2.00	3.15	6.28	3.97	0.93	1.30	0.76	1.16
7.00	13.32	3.28	1.26	3.97	0.93	0.64	1.32	1.48
7.00	13.30	3.28	1.26	3.97	0.93	0.64	1.30	1.50
7.00	8.62	3.30	1.88	3.97	0.93	0.68	1.20	1.54
7.00	6.10	3.31	2.51	3.97	0.93	0.76	1.11	1.59
7.00	4.90	3.34	3.14	3.97	0.93	0.75	1.10	1.58
7.00	4.71	3.29	3.14	3.97	0.93	0.82	1.03	1.56
7.00	3.13	3.26	4.40	3.97	0.93	0.94	0.92	1.46
7.00	2.42	3.23	5.65	3.97	0.93	0.96	0.85	1.37
7.00	10.48	3.31	1.57	3.97	0.93	0.66	1.29	1.50
7.00	7.24	3.31	2.20	3.97	0.93	0.70	1.16	1.54
7.00	1.91	3.16	6.91	3.97	0.93	1.04	0.77	1.28
7.00	12.93	3.28	1.26	3.97	0.93	0.68	1.33	1.48
7.00	6.14	3.32	2.51	3.97	0.93	0.75	1.14	1.59
7.00	3.82	3.30	3.77	3.97	0.93	0.86	1.00	1.54
7.00	2.74	3.26	5.03	3.97	0.93	0.95	0.90	1.42
8.00	12.97	3.26	1.26	3.97	0.93	0.53	1.13	1.19
8.00	8.42	3.30	1.88	3.97	0.93	0.55	1.10	1.38
8.00	5.78	3.34	2.51	3.97	0.93	0.65	1.11	1.67
8.00	4.37	3.32	3.14	3.97	0.93	0.74	1.02	1.92
8.00	3.02	3.22	4.40	3.97	0.93	0.80	0.84	1.74
8.00	2.26	3.12	5.65	3.97	0.93	0.87	0.73	1.54
8.00	10.26	3.28	1.57	3.97	0.93	0.54	1.12	1.29
8.00	7.05	3.32	2.20	3.97	0.93	0.58	1.11	1.50
9.00	10.29	3.27	1.26	3.97	0.93	0.44	1.03	1.36
9.00	6.40	3.33	1.88	3.97	0.93	0.50	1.04	1.59
9.00	4.11	3.33	2.51	3.97	0.93	0.68	1.01	2.31
9.00	3.17	3.26	3.14	3.97	0.93	0.74	0.88	2.10
9.00	2.57	3.28	3.77	3.97	0.93	0.78	0.88	1.94
9.00	13.94	3.24	0.94	3.97	0.93	0.43	1.04	1.28
9.00	8.04	3.32	1.57	3.97	0.93	0.46	1.06	1.48
9.00	4.71	3.37	2.20	3.97	0.93	0.67	1.10	2.46
9.00	3.57	3.29	2.83	3.97	0.93	0.72	0.94	2.14
9.00	5.32	3.41	2.04	3.97	0.93	0.61	1.17	2.30
9.00	1.35	3.02	6.28	3.97	0.93	1.02	0.67	1.51
9.00	3.04	3.31	2.83	3.18	0.94	0.56	0.91	N.A.
9.00	5.34	3.35	1.88	3.18	0.94	0.40	1.02	N.A.
9.00	2.15	3.16	3.77	3.18	0.94	0.64	0.76	N.A.
9.00	0.91	2.96	8.17	3.18	0.94	0.74	0.68	N.A.
9.00	0.73	2.92	10.05	3.18	0.94	0.75	0.68	N.A.
9.00	1.60	3.09	5.03	3.18	0.94	0.65	0.72	N.A.

TABLE 2. Continued.

REFERENCES

Bagchi, P. & Balachandar, S. 2002*a* Effect of free rotation on the motion of a solid sphere in linear shear flow at moderate *Re*. *Phys. Fluids* **14**, 2719–2737.

Bagchi, P. & Balachandar, S. 2002*b* Shear versus vortex-induced lift force on a rigid sphere at moderate *Re*. *J. Fluid Mech.* **473**, 379–388.

Bluemink, J. J., Lohse, D., Prosperetti, A. & van Wijngaarden, L. 2008 A sphere in a uniformly rotating or shearing flow. *J. Fluid Mech.* **600**, 201–233.

Bluemink, J. J., Van Nierop, E. A., Luther, S., Deen, N., Magnaudet, J., Prosperetti, A. & Lohse, D. 2005 Asymmetry-induced particle drift in a rotating flow. *Phys. Fluids* **17**, 072106.

Candelier, F., Angilella, J. R. & Souhar, M. 2004 On the effect of the Boussinesq–Basset force on the radial migration of a stokes particle in a vortex. *Phys. Fluids* **16**, 1765–1776.

Candelier, F., Angilella, J. R. & Souhar, M. 2005 On the effect of inertia and history forces on the slow motion of a spherical solid or gaseous inclusion in a solid-body rotation flow. *J. Fluid Mech.* **545**, 113–139.

Clift, R., Grace, J. R. & Weber, M. E. 1978 *Bubbles, Drops and Particles*. Academic.

Dandy, D. S. & Dwyer, H. A. 1990 A sphere in shear flow at finite Reynolds number: effect of shear on particle lift, drag, and heat transfer. *J. Fluid Mech.* **216**, 381.

Jenny, M., Bouchet, G. & Dušek, J. 2003 Nonvertical ascension of fall of a free sphere in a newtonian fluid. *Phys. Fluids* **15**, L9–L12.

Jenny, M., Dušek, J. & Bouchet, G. 2004 Instabilities and transition of a sphere falling or ascending freely in a newtonian fluid. *J. Fluid Mech.* **508**, 201–239.

Karamanev, D. G., Chavarie, C. & Mayer, R. C. 1996 Dynamics of the free rise of a light solid sphere in liquid. *AIChE J.* **42**, 1789–1792.

Kurose, R. & Komori, S. 1999 Drag and lift forces on a rotating sphere in a linear shear flow. *J. Fluid Mech.* **384**, 183–206.

Landau, L. D. & Lifshitz, E. M. 1987 *Fluid Mechanics*, 2nd edn. Butterworth-Heinemann.

Legendre, D. & Magnaudet, J. 1998 The lift force on a spherical bubble in a viscous linear shear flow. *J. Fluid Mech.* **368**, 81–126.

Lin, C., Peery, J. H. & Schowalter, W. R. 1970 Simple shear flow round a rigid sphere: inertial effects and suspension rheology. *J. Fluid Mech.* **44**, 1–17.

Magnaudet, J. & Eames, I. 2000 The motion of high-Reynolds number bubbles in inhomogeneous flows. *Annu. Rev. Fluid Mech.* **32**, 659–708.

Magnaudet, J. & Legendre, D. 1998 Some aspects of the lift force on a spherical bubble. *Appl. Sci. Res.* **58**, 441–461.

Magnaudet, J., Rivero, M. & Fabre, J. 1995 Accelerated flows past a rigid sphere or a spherical bubble. *J. Fluid Mech.* **284**, 97–135.

Mazzitelli, I., Lohse, D. & Toschi, F. 2003 On the relevance of the lift force in bubbly turbulence. *J. Fluid Mech.* **488**, 283–313.

Mougin, G. & Magnaudet, J. 2002 Path instability of a rising bubble. *Phys. Rev. Lett.* **88**, 014502.

Naciri, M. A. 1992 Contribution à l'étude des forces exercées par un liquide sur une bulle de gaz: portance, masse ajoutée et interactions hydrodynamiques. PhD thesis, L'Ecole Centrale de Lyon, Ecully, France.

Rastello, M., Mari, J., Grosjean, N. & Lance, M. 2009 Drag and lift forces on interface-contaminated bubbles spinning in a rotating flow. *J. Fluid Mech.* **624**, 159–178.

Rubinov, R. & Keller, J. B. 1961 The transverse force on a spinning sphere moving in a viscous fluid. *J. Fluid Mech.* **11**, 447–459.

Sakamoto, H. & Haniu, H. 1995 The formation mechanism and shedding frequency vortices from a sphere in uniform shear-flow. *J. Fluid Mech.* **287**, 151–171.

Shaw, W. L., Poncett, S & Pinton, J. F. 2006 Force measurements on rising bubbles. *J. Fluid Mech.* **569**, 51–60.

Van Nierop, E. A., Luther, S., Bluemink, J. J., Magnaudet, J., Prosperetti, A. & Lohse, D. 2007 Drag and lift forces on bubbles in a rotating flow. *J. Fluid Mech.* **571**, 439–454.

Veldhuis, C. H. J., Biesheuvel, A., van Wijngaarden, L. & Lohse, D. 2005 Motion and wake structure of spherical particles. *Nonlinearity* **18**, C1–C8.

Zhang, Z. & Prosperetti, A. 2005 A second-order method for three-dimensional particle simulation. *J. Comput. Phys.* **210**, 292–324.